



AFRL-RY-WP-TR-2010-1023



HIGH-EFFICIENCY AND HIGH-POWER MID-WAVE INFRARED CASCADE LASERS

Claire Gmachl

**Princeton University
Princeton Institute for the Science and Technology of Materials**

**AUGUST 2009
Interim Report**

Approved for public release; distribution unlimited.

See additional restrictions described on inside pages

STINFO COPY

**AIR FORCE RESEARCH LABORATORY
SENSORS DIRECTORATE
WRIGHT-PATTERSON AIR FORCE BASE, OH 45433-7320
AIR FORCE MATERIEL COMMAND
UNITED STATES AIR FORCE**

NOTICE AND SIGNATURE PAGE

Using Government drawings, specifications, or other data included in this document for any purpose other than Government procurement does not in any way obligate the U.S. Government. The fact that the Government formulated or supplied the drawings, specifications, or other data does not license the holder or any other person or corporation; or convey any rights or permission to manufacture, use, or sell any patented invention that may relate to them.

This report was cleared for public release by the Wright-Patterson Public Affairs Office and is available to the general public, including foreign nationals. Copies may be obtained from the Defense Technical Information Center (DTIC) (<http://www.dtic.mil>).

AFRL-RY-WP-TR-2010-1023 HAS BEEN REVIEWED AND IS APPROVED FOR PUBLICATION IN ACCORDANCE WITH ASSIGNED DISTRIBUTION STATEMENT.

*//Signature//

MATTHEW GRUPEN, Project Engineer
Aerospace Components Division

//Signature//

THOMAS R. NELSON, Chief
Aerospace Components Division

//Signature//

JAMES LOUTHAIN, Lt Col, USAF, Deputy Chief
Aerospace Components Division
Sensors Directorate

This report is published in the interest of scientific and technical information exchange, and its publication does not constitute the Government's approval or disapproval of its ideas or findings.

*Disseminated copies will show “//Signature//” stamped or typed above the signature blocks.

REPORT DOCUMENTATION PAGE				Form Approved OMB No. 0704-0188	
<p>The public reporting burden for this collection of information is estimated to average 1 hour per response, including the time for reviewing instructions, searching existing data sources, gathering and maintaining the data needed, and completing and reviewing the collection of information. Send comments regarding this burden estimate or any other aspect of this collection of information, including suggestions for reducing this burden, to Department of Defense, Washington Headquarters Services, Directorate for Information Operations and Reports (0704-0188), 1215 Jefferson Davis Highway, Suite 1204, Arlington, VA 22202-4302. Respondents should be aware that notwithstanding any other provision of law, no person shall be subject to any penalty for failing to comply with a collection of information if it does not display a currently valid OMB control number. PLEASE DO NOT RETURN YOUR FORM TO THE ABOVE ADDRESS.</p>					
1. REPORT DATE (DD-MM-YY) August 2009		2. REPORT TYPE Interim		3. DATES COVERED (From - To) 01 February 2007 – 31 July 2009	
4. TITLE AND SUBTITLE HIGH-EFFICIENCY AND HIGH-POWER MID-WAVE INFRARED CASCADE LASERS				5a. CONTRACT NUMBER	
				5b. GRANT NUMBER FA8650-07-1-7708	
				5c. PROGRAM ELEMENT NUMBER 69199F	
6. AUTHOR(S) Claire Gmachl				5d. PROJECT NUMBER ARPS	
				5e. TASK NUMBER ND	
				5f. WORK UNIT NUMBER ARPSNDBF	
7. PERFORMING ORGANIZATION NAME(S) AND ADDRESS(ES) Princeton University Princeton Institute for the Science and Technology of Materials Department of Electrical Engineering Princeton, NJ 08544				8. PERFORMING ORGANIZATION REPORT NUMBER	
9. SPONSORING/MONITORING AGENCY NAME(S) AND ADDRESS(ES) Air Force Research Laboratory Sensors Directorate Wright-Patterson Air Force Base, OH 45433-7320 Air Force Materiel Command United States Air Force				10. SPONSORING/MONITORING AGENCY ACRONYM(S) AFRL/RYPD	
				11. SPONSORING/MONITORING AGENCY REPORT NUMBER(S) AFRL-RY-WP-TR-2010-1023	
12. DISTRIBUTION/AVAILABILITY STATEMENT Approved for public release; distribution unlimited.					
13. SUPPLEMENTARY NOTES PAO Case Number: 88ABW 2010-0048; Clearance Date: 07 January 2010. This report contains color.					
14. ABSTRACT <p>Quantum cascade laser (QCL) performance continues to improve towards the requirements of applications such as infrared counter measures. However, key metrics, such as wall-plug efficiency (WPE), are still not fully met. DARPA's EMIL program continues to support progress in QCLs, and this report summarizes the Princeton team's work during Phase I of this program. Although the work systematically addressed all major facets of efficiency, the greatest advancements involved injection designs, which improved almost all efficiency components. Strain compensated QCLs with heterogeneous injectors produced low voltage defect. The active core consisted of interdigitated undoped and doped injectors followed by nominally identical optical transitions. The undoped injectors were designed with reduced voltage defect while the doped injector designs were more conventional. The measured average voltage defect was less than 79 meV. At 80 K, a 2.3 mm long, back facet high reflectance coated laser had an emission wavelength of 4.7 μm and output 2.3 W pulsed power with 19% peak WPE.</p> <p>Other QCLs emitting at 4.2 μm featured a low voltage defect and short injector with only four quantum wells. Devices with a voltage defect of 20 meV and a record voltage efficiency of 91% were demonstrated for pulsed operation at 180 K. Voltage efficiencies of greater than 80% were exhibited at room temperature. WPEs ranging from 21% at cryogenic temperatures to 5.3% at room temperature were achieved.</p> <p>Interface roughness effects were analyzed as in homogeneous broadening, explaining the temperature dependent QCL gain spectra and suggesting improved designs. Specifically, density-matrix theory revealed benefits from stronger coupling between injector and upper laser level that led to low-temperature pulsed QCLs nearing 50% WPE.</p>					
15. SUBJECT TERMS quantum cascade laser, mid-infrared radiation, wall plug efficiency, infrared counter measures					
16. SECURITY CLASSIFICATION OF:			17. LIMITATION OF ABSTRACT: SAR	18. NUMBER OF PAGES 70	19a. NAME OF RESPONSIBLE PERSON (Monitor) Matthew Grupen 19b. TELEPHONE NUMBER (Include Area Code) N/A
a. REPORT Unclassified	b. ABSTRACT Unclassified	c. THIS PAGE Unclassified			

Table of Contents

1.	Introduction	2
1.1.	Background	2
1.1.1.	Wallplug Efficiency in Quantum Cascade Lasers	2
1.2.	Scope of work	4
1.2.1.	Development of a “Global Quantum Cascade Laser Design Suite”	5
1.2.2.	Bandstructure Engineering of novel active regions	6
1.2.2.1.	Large band-offset unstrained InGaAs/AlInAs/AlAsSb and strained InGaAs/AlInAs structures	6
1.2.2.2.	Heterogeneous cascades as compensation for cross-core gradients	7
1.2.2.3.	Phonon Engineering	7
1.2.2.4.	In-plane periodicity in active region wells	8
1.2.3.	Bandstructure engineering of novel injectors and waveguides	8
1.2.4.	Novel, low-loss MWIR waveguides	9
1.2.5.	Improved thermal management	9
1.2.5.1.	Buried heterostructure (BH) lasers and epitaxial-side heat-sinking	9
1.2.5.2.	Use of short pulses with high average power	10
1.2.5.3.	Beam shaping and power scaling	10
1.3.	Outline of report	11
2.	Methods, Procedures and Results	11
2.1.	Conventional design Quantum Cascade lasers	11
2.2.	Low voltage-defect Quantum Cascade laser with heterogeneous injector regions	12
2.2.1.	Laser design and fabrication	12
2.2.2.	Experimental results and discussion	13
2.2.3.	Conclusion	16
2.3.	Quantum Cascade lasers with extremely low voltage defect of less than one longitudinal optical phonon energy	17
2.3.1.	Laser design and fabrication	17
2.3.2.	Experimental results and discussion	18
2.3.3.	Conclusions	21
2.4.	Quantum Cascade lasers with ultra-short injector regions	21
2.4.1.	Introduction	21
2.4.2.	Quantum Cascade laser with three injector wells	22
2.4.2.1.	Design and fabrication	22
2.4.2.2.	Results and discussion	23
2.4.2.3.	Device performance	26

2.4.3.	Quantum Cascade laser with two injector wells	27
2.4.3.1.	Design and fabrication	27
2.4.3.2.	Results and discussion	27
2.4.3.3.	Device Performance	30
2.4.4.	Conclusions	30
2.5.	Modeling of interface roughness in Quantum Cascade lasers and its impact on laser performance	31
2.5.1.	Inhomogeneous origin of the interface roughness broadening of intersubband transitions	31
2.5.2.	Role of interface roughness in the transport and lasing characteristics of Quantum Cascade lasers.	36
2.5.3.	Effective transit time in high performance Quantum Cascade lasers including the photon density	40
2.6.	Intersubband absorption loss in high performance Quantum Cascade lasers	41
2.7.	Lasing induced reduction of core heating in high wall plug efficiency Quantum Cascade lasers	43
3.	Discussion and recommendation	47
3.1.	Discussion of results	47
3.2.	Recommendation	48
4.	References	51

List of Figures and Tables

Fig. 1: Schematic of the conduction band structure of a short wavelength QC laser. The optical transition is indicated by the wavy arrow. The straight arrows indicate effects that contribute to the reduced WPE in QC lasers, such as thermionic emission, and electrons by-passing the active region via non-radiative effects, predominantly phonon scattering. The built-in voltage defect is shown as “ Δ ”.	3
Table I: Fundamental and practical limitations to the WPE and output power of QC lasers	4
Fig. 2: Conduction bandstructure design of a $\sim 4.6 \mu\text{m}$ wavelength QC laser employing lattice matched Sb-alloy barriers in the active region.	7
Fig. 3: Simulation of a representative QC laser operating in CW mode at 300 K heat sink temperature. The cross-sectional temperature maps represent various device layouts, left-to-right: epi-up & metal-clad, epi-up and buried heterostructure (BH), epi-down & metal-clad, and epi-down and BH.	10
Fig. 4: Light output – current – voltage characteristics of one of our best performing conventional QC lasers. The device was processed as BH laser with a cavity size of $7 \mu\text{m}$ wide and 5 mm long. The laser was mounted epitaxial-side down. The power refers to the total power of two as-cleaved facets. Heat sink temperature is 15°C . The WPE is 6% at its maximum, and 5.4% at peak output power.	11
Fig. 5: A portion of the conduction band structure with the moduli squared of the relevant wavefunctions. The optical transitions with design energies of 283 meV are denoted by the vertical black arrows. The doped and undoped injector regions are marked by the letters A and B, respectively. The shaded green and blue regions in the band diagram show the voltage defect for the two injectors. The extraction barrier marked “*”, indicates the first barrier for the design sequence detailed in the main text. The calculation is for an applied electric field of 82 kV/cm .	13
Fig. 6: (a) Pulsed EL spectra at 80 K from cleaved mesas as a function of current. Various pulse widths, 100 ns to $4 \mu\text{s}$, at a repetition rate of 79.9 kHz were used for the measurements. The inset shows a current-voltage plot for the same device at 80 K. (b) Spectral peak position (squares) and full width at half maximum (circles) of the fit Lorentzians versus applied current. The red data points are attributed to optical transitions following the undoped injectors and the black data points are attributed to optical transitions following the conventional injectors. The inset shows a characteristic double-peak Lorentzian fit of an EL spectrum.	14
Fig. 7: (a) Light-current measurements for a $15 \mu\text{m}$ wide, 1.23 mm long laser at different temperatures. The current-voltage curve for the laser at 80 K is also plotted. The inset shows the lasing spectrum of the device at room temperature and 1.1 times the threshold current. (b) Pulsed threshold current density, J_{th} , as a function of the heat sink temperature. The experimental data (squares), excluding 80 K, were fit with an exponential (dashed line), $J_{th} = J_o \exp(T/T_o)$, resulting in $T_o = 140 \text{ K}$.	15

Fig. 8: (a) Peak power (dashed) and wall-plug efficiency (solid) for the best performing, as-cleaved laser (15 μm x 1.44 mm). The device was operated with 90 ns pulses at a repetition rate of 5 kHz. The peak wall-plug efficiency (WPE) occurs at 5.6 kA/cm² is 14 % with a power of 2.0 W. (b) Peak WPE (black squares), peak power (red triangles), and power at peak WPE (red circles) as a function of temperature for the laser presented in Fig. 7a. 15

Fig. 9: (a) Pulsed wall-plug efficiency collected from one facet for several lasers versus cavity length. The squares are for uncoated lasers and the red triangles are for select devices that were HR coated on the back facet after initial as-cleaved measurements (black squares). (b) Measured pulsed threshold current density versus reciprocal cavity length at 80 K (filled squares). The dashed line is the result of a linear least squares fit. 16

Fig. 10: A portion of the conduction band structure along with the moduli squared of the relevant wavefunctions. Wavefunctions in bold illustrate the upper and lower laser levels of each active period. The optical transition, with a design energy of 298 meV, is depicted by vertical arrows. A very low voltage defect of ~36 meV is identified by E_d , for an applied electric field of 91 kV/cm. One can see the shortened injector regions, consisting of four quantum wells between each set of active regions. The calculation takes the free carrier density into account through a self-consistent solution of the Schrödinger and Poisson equations. 18

Fig. 11: Pulsed LIV measurements for a 3 mm long and 12 μm wide laser ridge at the indicated heat-sink temperatures. The light, showing output from both facets, is corrected for a collection efficiency of 75%. 19

Fig. 12: Peak WPE (squares), voltage efficiency at lasing threshold (circles), and voltage efficiency at peak WPE (triangles) versus heat-sink temperature for a 3 mm long and 12 μm wide laser ridge under pulsed operation. 19

Fig. 13: Threshold current density (black squares) and voltage defect at laser threshold (red circles) versus heat-sink temperature for a 3 mm long and 12 μm wide laser ridge under pulsed operation. The threshold current density values are fit with exponential curves, $J_{th} = J_0 \exp(T/T_0)$, resulting in two regions of differing characteristic temperature T_0 . A T_0 of 118 K exists at lower temperatures, while a T_0 of 174 K is obtained at higher temperatures. The discontinuity in the temperature performance occurs where the voltage defect at threshold corresponds to one LO-phonon (~34 meV). The inset shows pulsed laser spectra for the device at 1.1 times threshold for various heat-sink temperatures. 20

Fig. 14: QC structure with three injector wells and three active region wells. At 95 kV/cm the second energy level of one active region is in resonance with the down-stream upper laser state at this field. 23

Fig. 15: QC structure with three injector wells and three active region wells. The as-designed turn-on field is 114 kV/cm. 23

Fig. 16: Pulsed light–current–voltage (LIV) data of electroluminescence mesas for the three injector well QC structure. The area of the tested device is 0.033 mm². Pronounced negative differential resistance is seen at low temperature (a) and persists through room temperature (b). 24

Fig. 17: Light–current–voltage (LIV) data for a representative three injector well $10.4 \mu\text{m} \times 3 \text{ mm}$ ridge laser device. As seen in (a), negative differential resistance (NDR) is observed, but only at elevated temperatures. From (b), we see that the NDR appears only for $J_{\text{th}} > J_{\text{NDR}}$, i.e. here for $T_{\text{sink}} \gtrsim 130 \text{ K}$. Because of the NDR, we observe two thresholds for $T_{\text{sink}} = 130 \text{ K}$ and slightly above. The comparison of LIV data from this laser device and EL data from Fig. 16b, as in (c), shows the effect of cavity photon density on the current–voltage behavior. 25

Fig. 18: LIV data near the transition $J_{\text{th}} > J_{\text{NDR}}$, here for $T_{\text{sink}} = 130$ and 134 K . Different slope efficiencies are observed before and after the band configuration that results from the presence of stimulated emission. No significant change in slope efficiency is observed before and after the NDR point. 26

Fig. 19: (a) Representative normalized spectra of the three injector well structure for $T_{\text{sink}} = 78 \text{ K}$ and 302 K near threshold. Characteristic temperature T_0 (b) and pulsed wall-plug efficiency (c) for a $10.4 \mu\text{m} \times 3 \text{ mm}$ ridge laser device. 26

Fig. 20: (a) QC structure with two injector wells and three active region wells. NDR is observed in this structure at $E_{\text{field}} = 103 \text{ kV/cm}$, shown in (a). The designed turn-on field is 128 kV/cm , shown here in (b). Also, an increase in differential resistance is seen in device data consistent with a reconfiguration of the band alignment where the upper laser state is in resonance with the injector ground state, as in (c), near $E_{\text{field}} = 138 \text{ kV/cm}$. 28

Fig. 21: Pulsed LIV data for a representative two injector well $7.5 \mu\text{m} \times 3 \text{ mm}$ BH laser device. Two “turn-off” features are seen, one occurring with constant voltage and one with constant current. Pulse instabilities in the light power are also evident at lower temperatures. Because of these instabilities, output power is highest at elevated temperatures. The data shown here are for sampling averaged over ~ 15 pulses. 29

Fig. 22: (a) Representative normalized spectra of the two injector well structure for $T_{\text{sink}} = 79 \text{ K}$ and 300 K near threshold. Characteristic temperature T_0 (b) and pulsed wall-plug efficiency (c) for a two injector well $7.5 \mu\text{m} \times 3 \text{ mm}$ BH laser device. 29

Fig.23: **a.** Electron density spectrum of the states mixed due to interface roughness. **b.** Snapshot of a typical random mixed wave function. 34

Fig.24:**a** Left hand side: allowed transitions between the states mixed by interface roughness. Right hand side: Absorption and emission between two subbands and their populations as function of energy. **b.** Gain and absorption spectra of the IST in QC lasers for different temperatures. 35

Fig.25: Energy diagram of a $4.7 \mu\text{m}$ QCL with relevant transition times indicated by the solid arrows and dephasing times indicate by the dashed arrows. 37

Fig.26: The gain coefficient as a function of energy level splitting $2\hbar\Omega_c$ in QCL of Fig.25. 40

Fig.27: The shape of laser linewidth for different detuning between injector and upper laser level. 40

Fig. 28: Effective transit time as a function of the dimensionless coupling parameter ($4\Omega_c\tau_\perp\tau_u$) for the structure shown in Fig. 25.	41
Fig. 29: (a) Conduction band diagram for the low voltage defect QC laser design; (b) conduction band diagram for the QC laser design with strong coupling. Highlighted transitions make significant contributions to intersubband absorption loss.	42
Fig. 30: (a) Calculated intersubband absorption loss for the low voltage defect and strong coupling designs as functions of the transition energy at two different temperatures. (b) Measured threshold current density versus reciprocal cavity length at 80 K for the two designs.	43
Fig. 31: Continuous wave voltage (solid, black), light (dash, red), and WPE (dot-dash, blue) versus current curves for the high efficiency device at a heat sink temperature of 80 K. The power and WPE values are reported for both facets.	44
Fig. 32: Threshold current versus heat sink temperature data of the high efficiency device for CW (red circles) and pulsed (blue squares) operation. The inset shows the thermal resistance, R_{TH} , calculated from the difference in threshold currents versus temperature.	44
Fig. 33: Light versus pulsed current for measurements below (blue) and above (red) CW threshold. The blue and red arrows show the direction of the increase in the magnitude of the current pulses below and above CW threshold respectively. The inset shows a schematic of the current pulses supplied to the device in addition to the DC current. The lasing threshold, $\delta I_{pulse, Th}$, is indicated for both measurements.	46
Fig. 34: Plot of core temperature versus DC input power. The blue squares are for the experimental results; the blue, solid line is for calculations including the WPE; and the red, dashed line is for calculations with zero WPE for all input powers. The power corresponding to CW threshold, $P_{DC, Th} = 1.8$ W, is marked by the vertical, dashed line. There is excellent agreement between experiment and the calculations; the only free parameter is the initial core temperature which was matched to the experiment.	46
Fig. 35: (A) A portion of the conduction band diagram of the ultra-strong coupling QC laser design. The pairs of states in red have a coupling strength of ~ 20 meV. Starting from the first barrier in the injector, the layer sequence with individual thickness in nanometer is: 2.3/2.8/2.6/2.2/2.1/1.8/1.8/1.5/1.3/1.2/1.0/4.2/1.2/3.9/1.4/3.3, where the InAlAs barrier layers are in bold, the InGaAs well layers are in roman. (B) Electroluminescence spectra of the QC structure with extracted full width at half maximum. (C) Exemplary laser spectrum. (D) Pulsed light-current-voltage measurements for an as-cleaved $13.5 \mu\text{m}$ wide, 2.9 mm long QC laser at various heat sink temperatures. Measured single-facet optical power is doubled for two facets and corrected for optical collection efficiency. (E) Wall-plug efficiency extracted from the experimental results in (D).	49

Acknowledgement

I would like to acknowledge the exceptional teamwork and outstanding contributions of all members of our team at AdTech Optics, Johns Hopkins University, the Naval Research Labs, Princeton University, and the University of Maryland Baltimore County. My special thanks goes out to our graduate and undergraduate students as well as post-doctoral researchers involved in this project. Many nights spent in the labs and on the computers served not only to raise the performance of QC lasers to new heights, but they also influenced your future careers.

I would like to thank Dr. Thomas R. Nelson and Dr. Matthew E. Grupen and their staff for checking in on us always with encouragement and always seeing and pointing out the positive aspects of our work. Their positive guidance and intelligent questions proved invaluable many times over. I would like to also acknowledge our managers at DARPA, Dr. Mark Rosker, in particular, and his collaborators on the EMIL project, including the teams conducting the review meetings. Their constant challenges and interesting questions proved most useful and enlightening. The results of the EMIL program would not have reached the level they did if not for their untiring behind-the-scenes work.

I would also like to acknowledge our competing teams in the EMIL program. We have shared more insights and data with each other than will ever be known publicly, and the fairness and excitement in pursuing a common goal was most enjoyable.

Finally, posthumously, my heart-felt gratitude to Dr. Henryk Temkin, who started the EMIL program so strongly and led it far longer than his illness seemingly allowed it. His dedication to his projects was most palpable, and in this he inspired many of us to work harder and more sincerely. He will be missed.

Summary

High-Efficiency and High-Power Mid-Wave Infrared Quantum Cascade Lasers

Quantum Cascade (QC) lasers continue to see rapid performance improvements driven mainly by applications such as chemical trace gas sensing or infrared counter measures. Especially for the latter, the laser performance in output power, wall-plug efficiency (WPE), and beam profile, however, is still trailing both its desired characteristics and its modeled potential. The ongoing DARPA EMIL program – of which the here-reported work is a part of – has done much to change this status quo, and initiated research and development for high power, high WPE, and superior beam profile QC lasers. This report summarizes our team's main activities and results during the Phase I performance period.

In our initial approach to the Tasks under the EMIL program we closely followed our planned multi-faceted approach, addressing individual challenges and open questions regarding the various components of the WPE. We addressed essentially all Phase I issues, eliminating some as not essential, and/or resolving others. Ultimately, the biggest innovation and the greatest advancements came from the work on innovative injection designs, which improved voltage efficiency, internal efficiency, and also current efficiency (at low temperatures); only the optical efficiency was not systematically improved.

We demonstrated strain compensated QC lasers that employ heterogeneous injector regions for low voltage defect operation. The active core consisted of interdigitated undoped and doped injectors followed by nominally identical wavelength optical transitions. The undoped injector regions were designed with reduced voltage defect while the doped injectors are of a more conventional design. The measured average voltage defect was less than 79 meV. At 80 K, a 2.3 mm long, back facet high reflectance coated laser had an emission wavelength of 4.7 μm and output 2.3 W pulsed power with a peak wall-plug efficiency of 19%.

We demonstrated a QC laser emitting at 4.2 μm featuring a low voltage defect and short injector with only four quantum wells. Devices with a voltage defect of 20 meV, well below the energy of the longitudinal optical phonons, and a voltage efficiency of 91%, a record value for QC lasers, were demonstrated for pulsed operation at 180 K. Voltage efficiencies of greater than 80% were still exhibited at room temperature. Overall performance showed WPE's ranging from 21% at cryogenic temperatures to 5.3% at room temperature.

The impact of the interface roughness on intersubband transitions in quantum wells was analyzed as an inhomogeneous broadening due to localization rather than a traditional scattering process. The results offered a simple explanation for the temperature dependent spectra of gain and absorption in QC lasers and pointed the way for improved designs. In particular, a density-matrix based theory of transport and lasing in QC lasers revealed that the large disparity between luminescent linewidth and broadening of the tunneling transition changes the design guidelines to favor a stronger coupling between injector and upper laser level.

These new design guidelines ultimately led to low-temperature pulsed QC lasers that demonstrated the potential for QC lasers operating with 50% WPE.

1. Introduction

1.1. Background

Through the roughly 15 years since its invention the Quantum Cascade (QC) laser has seen rapid performance improvements mainly driven by genuine scientific curiosity as well as its initial use for chemical trace gas sensing. Yet for other applications, such as infrared counter-measures, its practical performance in output power, wall-plug efficiency (WPE), and beam profile is still trailing its modeled potential. The ongoing DARPA EMIL program – of which the here-reported work is a part of – has done much to change this status quo, and initiated research and development for high power, high WPE, and superior beam profile QC lasers. This report summarizes our team's main activities and results during the Phase I performance period.

Quantum Cascade lasers are especially well suited for high power output since the cascading scheme generates many photons per injected electron, hence compensating for the lower photon energy as compared to shorter wavelength diode lasers.[1] They also have excellent spectral coverage in the mid-wave infrared (MWIR) as the emission wavelength can be fixed by quantum well design rather than material choice. Furthermore, with their small linewidth enhancement factor and robustness against filamentation, QC lasers are expected to have superior far-field patterns and excellent high speed modulation characteristics.[2] Nevertheless, the WPE is not naturally high for reasons that will be discussed in more detail in section 1.1.1., which manifests itself in two unfortunate ways:

- (i) As much of the electrical power is dissipated as heat, a substantial external cooling system is needed, whereas, ideally the laser would cool itself by emitting light, as is the case with conventional, near-IR, high WPE semiconductor lasers.
- (ii) With limited capacity for heat dissipation, and exacerbated by poor thermal conductivity, the laser core heats up, degrading practically all laser parameters and consequently requiring more electrical power, hence driving a positive thermal feedback cycle that further reduces the WPE, reduces the output power, and ultimately shuts down the laser (or even destroys it).

1.1.1. Wallplug Efficiency in Quantum Cascade lasers

The lower efficiencies of QC lasers in general can be understood from the model of WPE, which for “well-behaved” QC lasers (i.e. QC lasers designed for high performance) is calculated from a straightforward rate equation model as:

$$\eta_{wp} = \left(\frac{E_\gamma n_p}{n_p (E_\gamma + E_\Delta) + qV_s} \right) \left(\frac{\alpha_m}{\alpha_w + \alpha_m} \right) \left[\left(\frac{\tau_{up}}{\tau_{up} + \tau_{inj}} \right) (\xi_{inj}) \right] \left(\frac{J - J_{th}}{J} \right), \text{ with} \quad (1a)$$

$$J_{th} = \frac{1}{\tau_3 (1 - \tau_2 / \tau_{32})} \left[\frac{\epsilon_0 n_{eff} \lambda L_p (2\gamma_{32})}{4\pi q z_{32}^2} \frac{\alpha_{tot}}{\Gamma} + q n_{2D} e^{-\Delta/k_B T} \right] \quad (1b)$$

Here, n_p is the number of active region stages, E_γ the photon energy, E_Δ the non-radiative energy drop per stage, q the electron charge, V_s the residual voltage of the structure due to the series resistance in contacts and waveguide, J and J_{th} are the instantaneous current and threshold current density, respectively, α_m and α_{tot} are the mirror and total (mirror plus waveguide α_w)

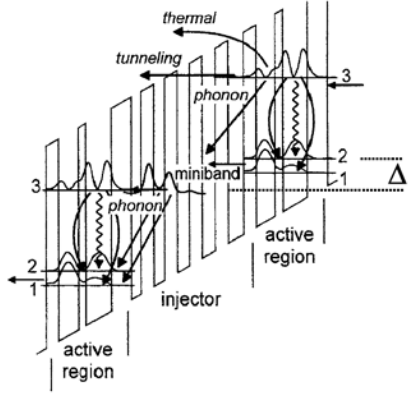


Fig. 1: Schematic of the conduction band structure of a short wavelength QC laser. The optical transition is indicated by the wavy arrow. The straight arrows indicate effects that contribute to the reduced WPE in QC lasers, such as thermionic emission, and electrons by-passing the active region via non-radiative effects, predominantly phonon scattering. The built-in voltage defect is shown as “ Δ ”.

losses, respectively, ξ_{inj} is the current injection efficiency into the upper laser level, and $\tau_{up} = \tau_3(\tau_{32} - \tau_2)/\tau_{32}$, with τ_3 , τ_{32} , and τ_2 being the total upper laser-level lifetime, the scattering time between upper and lower levels, and the lower level lifetime, respectively; τ_{inj} is the electron transit time through the injector; ϵ_0 is the vacuum dielectric constant, n_{eff} the effective refractive index of the mode, λ the emission wavelength, L_p the thickness of one laser active region with injector, $2\gamma_{32}$ the gain bandwidth, z_{32} the optical dipole matrix element for the laser transition, Γ the optical mode confinement factor for the entire stack of active regions and injectors, n_{2D} the sheet carrier density, T the local temperature, and k_B the Boltzmann constant.

As can be seen from Eq. (1), several interrelated effects contribute to the reduced WPE in QC lasers. The most important ones are schematically shown in Fig. 1, and summarized as follows (*Italics have been added to reflect new insight gained from the here performed work.*):

- (i) The voltage defect, $n_p \times E_\Delta$, in the active waveguide core, that is necessary to inhibit thermal repopulation of the lower laser levels from the downstream electron reservoirs, and the series resistance in the cladding layers and contacts, are sources of energy loss that is not recuperated optically.
- (ii) The waveguide loss, (*at the beginning of the program thought to be*) dominated by Drude (*i.e.*, free-carrier) absorption *and resonant intersubband absorption* in the active, separate-confinement, and cladding layers, is generally high.
- (iii) A non-unity internal carrier injection efficiency results from nonradiative and thermionic processes, *and is also influenced by roughness scattering.*
- (iv) The laser threshold current is generally high in QC lasers due to the very short non-radiative scattering lifetime for the upper laser level, ensuing small $z_{32}^2 \tau_3$ product, and large optical loss, *and – as we will see – reduced current injection efficiency into the upper laser level.*

Practically all of these parameters are temperature dependent and contribute to an exponential degradation of the WPE with increasing temperature. Examples include the exponential speed-up of non-radiative longitudinal optical (LO) phonon scattering, the thermal repopulation of the lower laser level from the down-stream extrinsic electron reservoir (across Δ), and others.

Furthermore, the interconnection of these effects drives a positive thermal feedback loop, in which a rise in laser core temperature induces an increased laser threshold that leads to an increase in dissipated power and back to a further rise in the laser core temperature. In addition to these primary, fundamental concerns, several more practical limitations and effects also reduce the WPE. Table I, below, gives an overview of the fundamental and practical impediments to the WPE and high output power of QC lasers.

Table I: Fundamental and practical limitations to the WPE and output power of QC lasers

Fundamental limitations:

- Low $z_{32}^2 \cdot \tau_3$ product
- Low internal quantum efficiency
- Thermionic emission into continuum
- Internal carrier leakage
- Voltage defect in active core (“ Δ ”)
- Waveguide loss from free carrier absorption
- Thermal degradation of laser performance
- Positive feedback on thermal effects
- Large beam divergence
- Single-device power ceiling from thermal roll-over and hole burning
- *Waveguide loss from resonant intersubband absorption*
- *Interface roughness scattering impacting electron transport and tunneling*

Practical limitations:

- Complexity and size of QC design space
- Incomplete knowledge of material parameters
- Excessive voltage defect in waveguide & contacts
- Excessive waveguide loss from free carrier absorption resulting from increased doping level tolerance
- Waveguide loss from scattering on imperfections
- Imperfections in laser packaging leading to thermal barriers
- Pointing instabilities from waveguide imperfections

1.2. Scope of work

It is evident from the discussion above that the complex challenge of raising the WPE to the much desired $\geq 50\%$ must necessarily be met by simultaneously addressing a variety of issues, especially the ones discussed above. Following Eq. 1a one may view the WPE as a product of four efficiencies:

$$\text{Voltage efficiency} \times \text{Optical efficiency} \times \text{Internal efficiency} \times \text{Current efficiency} \quad (2)$$

In order to bring the total efficiency to 50% or above, each of the sub-efficiencies need to be at least 85%; if one is less, the others need to compensate. Therefore, we commenced our work with a multi-faceted approach to address all of these components, through focusing on the individual issues of Table I. Focusing on only a single efficiency component would not be sufficient to reach the goal, nor would it show much impact – especially on the background of highly variable values of the other efficiency components. We commenced with a suite of interconnected strategies, some evolutionary (but nonetheless necessary) and most revolutionary. Rather than being “disjoint”, each component of this multi-faceted approach was designed to work in close interrelationship with all others. Through the course of the performance period, some issues became resolved or were identified as not essential, and new insight was gained to chart the path forward.

In the following we will briefly discuss the various strategies that were worked on; in the later section we focus in greater detail onto the most successful strategies, as well as their results.

1.2.1. Development of a “Global Quantum Cascade Laser Design Suite”

High performance QC lasers operated in continuous wave (CW) mode at room temperature (RT) are described by three models at three different length scales:

- The quantum mechanics model, which – at the nanometer scale – describes radiative and non-radiative electron scattering as well as the energy levels and wavefunctions,
- The optical waveguide model, which – at the micrometer scale – covers optical loss, confinement, and radiation patterns, and
- The thermal and heat dissipation model, which – at the millimeter scale – predicts steady state temperature profiles and cooling requirements.

Due to the different length scales, these models are often separate models, which makes designing high performance QC lasers inefficient and potentially error prone. An optimization at one length scale and in one model may result in a sub-optimal solution at the other length scales. Therefore, at the beginning of the project we consolidated our team’s various modeling tools, together with commercial modeling tools, and verified them across team members; in effect, we assembled a *Quantum Cascade Laser Design Suite* that for the remainder of the program allows efficient modeling of QC lasers at all length scales.

Through the course of the project, team member Johns Hopkins University furthermore developed refined models for roughness scattering that went deeper into microscopic (“nanoscopic”) device modeling than originally anticipated.

The suite of *Quantum Cascade Laser Design modeling tools* was applied to four specific tasks:

- (i) The program suite was used to extract material parameters from QC lasers that are essential to successful laser design and optimization, but are generally difficult to assess or not known to the required accuracy. Aside from the anticipated use of the modeling tools for such parameters as thermal conductivity of complex heterostructures, the close comparison between modeling and experiment also allowed us to – mid-program – revise our material parameters, such as effective mass and band-offset, for strained compositions of InGaAs/AlInAs, which in turn resulted in the design of improved QC lasers towards the second half of the project period.
- (ii) The program suite was used as is continued to be used as an analytical tool to examine existing and envisioned QC lasers in a most comprehensive way to fully understand the devices, and hence point the way to improved laser design.
- (iii) The program suite is being used to simulate series of experiments rather than experimentally working through them, which saves time and resources. An example would be to determine the effect of specific processing parameters such as side-wall coatings or facet coatings. Some device optimization can be done much faster on the computer followed by experimentation to verify the optimum conditions.
- (iv) Finally, automated computer routines allow for unassisted or marginally user-assisted QC laser optimization. These optimizing routines are essential to probe the widest parameter space possible. It was, however, found that human intuition of an

experienced QC laser designer, together with several days of computer-aided design work, comes very close to optimum conditions of a specific design task.

Aside from fully modeling QC lasers in classic ridge waveguide configurations, our QC laser design suite is also capable of modeling complex optical cavities, such as large area photonic crystal distributed feedback (PCDFB) cavities, or on-chip spectral beam combined (OSBC) QC lasers.

1.2.2. Bandstructure Engineering of novel active regions

1.2.2.1. Large band-offset unstrained InGaAs/AlInAs/AlAsSb and strained InGaAs/AlInAs structures

A meticulous, error-free, optimized quantum design of the active region is crucially essential for high performance QC lasers. In particular, the MWIR poses specific complications due to the large optical transition energies (250 – 350 meV). The well-studied and well-behaved InGaAs/AlInAs heterostructure lattice matched to InP provides for only about 500 meV of conduction band offset, which is not enough for a high-performance 250 meV ($\sim 4.8 \mu\text{m}$ wavelength) or higher energy QC laser; both, loss of actual quantum confinement of the upper laser level and thermionic emission into the continuum above the quantum wells degrade the laser performance by increasing carrier leakage and lowering the internal quantum efficiency.

Therefore, a larger band-offset heterostructure must be employed. While exotic heterostructures (such as GaSb- or GaN-based) may be viable long-term propositions, InP-based heterostructures have advantages associated with the high thermal conductivity of this type substrate and waveguide material, as well as the maturity of the InGaAs/AlInAs/InP material system and QC laser designs, which are grown equally well by MBE and MOCVD.

At the beginning of this work, we chose two heterostructure subsystems that seemed the most promising for delivering high WPE within the timeframe of the proposed work, unstrained and fully lattice-matched InGaAs/GaAsSb/AlInAs/AlAsSb/InGaAlAsSb (not all of these alloys in the same structure) and strain-compensated InGaAs/AlInAs, both grown on InP substrates.[3] Advantages of the Sb-alloy heterostructure are its large band-offset (~ 800 meV to the X-valley minimum in InGaAs/AlAsSb, and ~ 1.5 eV at the Γ point that reduces the density of states for internal absorption) and its ability to be grown lattice matched on InP; strained InGaAs/AlInAs provides a band-offset of up to ~ 750 meV, and has repeatedly proven suitable for high performance QC lasers.

Figure 2 shows the bandstructure design of a $\sim 4.6 \mu\text{m}$ wavelength QC laser employing lattice matched Sb-alloy barriers in the active region while retaining AlInAs barriers in the injector region. To our knowledge, such a hybrid design has not been investigated previously.

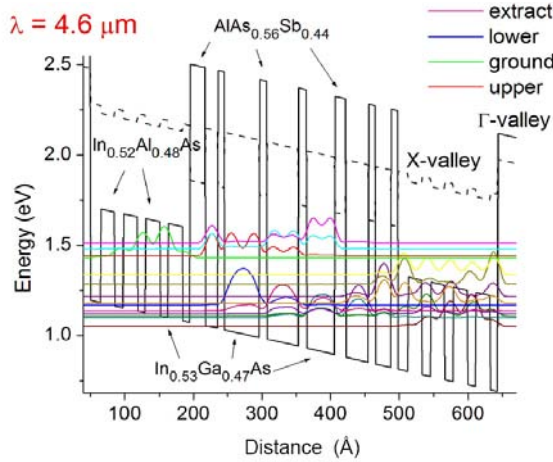


Fig. 2: Conduction bandstructure design of a $\sim 4.6 \mu\text{m}$ wavelength QC laser employing lattice matched Sb-alloy barriers in the active region.

We designed several QC laser structures, but ultimately failed in realizing them in the lab, as several, some severe, mechanical failures in our Sb-based growth reactor did not allow us to grow sufficiently high quality heterostructure material. We focused therefore on the growth of strain-compensated InGaAs/AlInAs, which resulted in high quality material.

1.2.2.2. Heterogeneous cascades as compensation for cross-core gradients

When operated in continuous wave mode the core of a QC laser heats up significantly, sometimes up to $\sim 100\text{K}$ above the heat sink and laser substrate temperature, resulting in pronounced thermal gradients even across the core stack of active regions and injectors.[4] Furthermore, the requirement for high optical power and the spatial extent of both the optical mode and stack of active regions and injectors leads to partial hole-burning in some of the active regions. As a result, active regions and injectors at the center of the QC laser core stack experience a different environment from active regions and injectors at the beginning and end of the stack.

To mitigate the detrimental effects of these cross-sectional gradients, we proposed to design heterogeneous cascades,[12] in which each active region is designed according to its place in the stack and hence the local environment it is subjected to. Nevertheless, careful modeling – using our Global QC Laser Design Suite (see section 1.2.1 above) – and comparison to experiments showed that the effect is negligible over other more pressing factors impacting QC laser performance, and the proposed design was not longer pursued.[5]

1.2.2.3. Phonon Engineering

The internal quantum efficiency of QC lasers, their gain, their threshold current density, and consequently also their WPE and output power greatly depend on the product $z_{32}^2 \tau_3$. These factors are two of the most essential quantum design parameters for QC lasers. In this sub-project, we intended to rigorously maximize the $z_{32}^2 \tau_3$ product by phonon engineering with two new features incorporated: First, step quantum wells grown from InGaAlAsSb alloys that allow optimization of the wavefunction overlap and an increase in the dipole matrix element; and second, by exploiting the mass non-parabolicity of this material system we intended to slow down the LO-phonon scattering from the upper laser state (at high in-plane wave-vectors) while speeding up the scattering out of the lower state (τ_2).

After initial calculations and also observing the experimental difficulties with the Sb-based material system, and given the short time frame of the proposed work, we ultimately abandoned this course of research in favor of a more detailed modeling and deeper understanding of the relevant parameters in the conventional, binary strained InGaAs/AlInAs system.

1.2.2.4. In-plane periodicity in active region wells

An important reason for the low internal quantum efficiency in QC lasers can be found in the ultra-fast (\sim ps) relaxation time for LO-phonon scattering between the laser subbands, which in turn results from the continuity of the parabolic subbands. Prompted by experimental findings of high resolution scanning tunneling microscope images of InGaAs/AlInAs heterostructures,[6] that showed weak in-plane periodicity remotely resembling self-organization we evaluated the introduction of an in-plane periodicity into the QC laser active region quantum wells, which could be in form of shallow quantum dots or anti-dots, to reshape the subbands in appropriate fashion and consequently slow down scattering from the upper laser level and/or speed up scattering from the lower laser level.

Contrary to other work on quantum dot (QD) QC structures, this approach does not rely on an in-plane quantization of the energy spectrum as would be obtained from conventional QDs.[7] Rather, this approach relies on opening small (5 – 10 meV) gaps in the subband structure at energies close to one LO phonon below the upper laser level, and on reshaping the density of states in the subbands for faster depopulation of the lower laser level. Ultimately, the effect was found – by meticulous modeling – to be too small to have a significant impact on the WPE, also given the perceived difficulty in actually fabricating the required in-plane periodicity.

1.2.3. Bandstructure engineering of novel injectors and waveguides

Conventional high performance QC lasers contain in each stage of active region and injectors a reservoir of electrons that is introduced by extrinsic doping and serves to feed each downstream active region with electrons and also locally stabilizes the applied electric field. During laser operation, these extrinsic electrons mostly reside in the ground state of the injector and the upper laser level of each stage. The quasi Fermi-level of each of these reservoirs must lie far enough below the lower laser level of the previous active region to prevent thermal repopulation of the former and subsequent collapse of population inversion. Hence, there is an in-built (by design) voltage drop “ Δ ” between adjacent stages, as shown in Fig. 1. This voltage defect, multiplied by the number of stages, imposes one of the most challenging limitations on the maximum WPE for a QC laser.

A significant effort of this project was therefore spent designing new injector regions that eliminate the impact of the electron reservoir and significantly reduce the voltage defect, even to one LO-phonon energy or less. It is essential that such injectors be highly transparent for electrons, essentially allowing for quasi-coherent or ultra-fast electron transport across the stages. Such behavior is provided by a design with short injectors and electron wavefunctions spanning stably across the injector and its two adjacent active regions for a large range of applied electric fields. In fact, much of the improvement in voltage efficiency stems from our improved injector designs. We will discuss the work on new injectors in far more detail in chapter 2 of this report.

In addition to reducing the voltage defect in the active laser core, the waveguide and contact regions have also been re-examined to identify any remaining voltage defects, which in turn will be eliminated or reduced to their fundamental and/or practical limits.

1.2.4. Novel, low-loss MWIR waveguides

The optical loss, especially the intrinsic (free carrier induced) waveguide loss, is one of the key factors that limit the threshold current, output power, and WPE of QC lasers. Therefore, any serious effort to advance the performance must include a comprehensive analysis and optimization of the waveguide losses. In this project, use of buried heterostructure (BH) waveguides was aggressively pursued, which results in intrinsically lower waveguide loss compared with metal-clad QC lasers. Doping levels in all layers were kept at the minimum, and – whenever possible – multiple QC laser wafers were grown to explore optimized doping levels, to counter excessive free-carrier absorption. Furthermore, new insights were gained from both experimental and modeling work, which – over the course of the project – shifted the focus from plain Drude (free-carrier) loss to resonant intersubband loss.

1.2.5. Improved thermal management

1.2.5.1. Buried heterostructure (BH) lasers and epitaxial-side heat-sinking

A large fraction of the electrical power that is dissipated inside a QC laser is dissipated inside the active region core. This is exacerbated by the fact that the laser core also has the lowest thermal conductivity of all the materials in the layered structure. To address these detrimental heating effects on the WPE and output power, it is clearly of utmost importance that we find means to efficiently cool the laser core. Two interrelated strategies have been followed.

First, devices for CW, RT operation are routinely fabricated as BH lasers employing InP lateral regrowth; the InP thermal resistance is significantly less than for the most popular conventional approach of employing a thin insulation layer (SiN or SiO₂) covered by thick electroplated gold. Employing a buried heterostructure design essentially provides heat removal from the laser core on all four sides as opposed to other designs that extract the heat mainly through the substrate, and depending on the thickness of the gold layer also from the top.

Second, in addition to extracting the heat efficiently it is highly advantageous to provide a heat sink very close to the laser. Hence the lasers are mounted epitaxial-side down on thermal heat sinks. Figure 3 shows the simulation of a representative QC laser operating in CW mode at 300 K heat sink temperature. The cross-sectional temperature maps represent various device layouts: buried heterostructure or metal-clad, and epi-side-up or -down mounted. To no surprise, the epitaxial-side down mounted buried heterostructure laser consumes the least electrical power at the lasing threshold and retains the coolest laser core. The clear reduction in electrical power consumed is a direct consequence of the thermal feedback cycle that QC lasers experience; reduced laser core temperature benefits from both improved heat-sinking and reduced dissipated power.

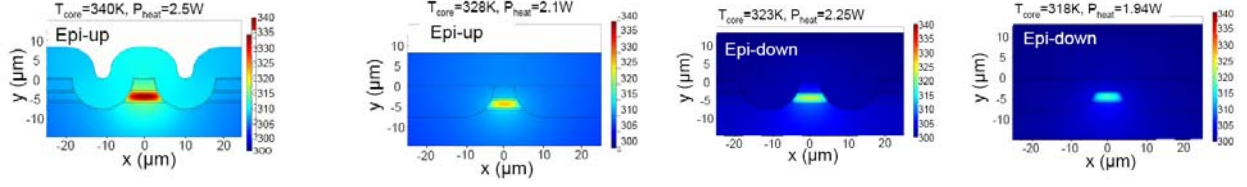


Fig. 3: Simulation of a representative QC laser operating in CW mode at 300 K heat sink temperature. The cross-sectional temperature maps represent various device layouts, left-to-right: epi-up & metal-clad, epi-up and buried heterostructure (BH), epi-down & metal-clad, and epi-down and BH.

Finally, an important – practical rather than fundamental – factor in the overheating of QC lasers (even for epitaxial-side heat sinking) is imperfect bonding to the heat spreader and cold surface of the heat sink. Through collaborators of our team member at the Naval Research Labs, we have conducted acoustic imaging studies on epitaxial-side bonded QC lasers to identify hidden gaps and voids at the bonding interface. The result was new insights into refined bonding parameters and optimized bonding recipes.

1.2.5.2. Use of short pulses with high average power

One of the most significant factors limiting the WPE in QC lasers is the high threshold current density. In state-of-the-art devices at 300 K, the latter often represents half or more of the maximum allowed current density, which is limited either by thermal roll-over or by Stark effect roll-over [5], i.e. by the available free carrier density. Nevertheless, the same lasers operate in pulsed mode with significantly lower thresholds and higher peak output powers.

Therefore, aside from developing CW QC lasers we also evaluated our QC lasers for operation with short pulses (~ 100 ns) and high average duty cycles ($\sim 30\%$), which results in very high average powers that are generated when the lasers are operated far above threshold [8]. We emphasize that for most applications such as IR countermeasures, frequencies exceeding ≈ 300 kHz are effectively CW, and hence very-rapid-pulse operation with high average power has no inherent disadvantage from a systems and applications point of view.

Operating the lasers in pulsed, high average power mode also has other advantages, including a new optimal operating point that allows for a larger number of active region stages (e.g. 40–45 vs. ~ 30), higher core doping, and shorter cavities with reduced facet reflectivity, albeit this detailed work has to wait until future research.

1.2.5.3. Beam shaping and power scaling

A single QC laser with high ($\geq 50\%$) WPE should readily emit ≥ 1 W of optical power, as most parameters that are optimized for a high WPE also result in a high output power. Nevertheless, for realistic IRCM systems up to 10 W or more of optical power are ideally needed.

Furthermore, the beam must have high brightness and low divergence in both axes. We originally proposed and commenced to explore two strategies to achieve these goals. First, photonic-crystal distributed-feedback (PCDFB) QC lasers that use diffraction by a two-dimensional grating to maintain optical coherence and suppress filamentation in very wide gain stripes; [9] and, second, on-chip spectral beam combining (OSBC) that couples multiple individual narrow-ridge lasers into a single waveguide, with no substantial sacrifice of power or beam quality. [10] Both strategies are still under consideration for future systems development.

1.3. Outline of report

The above discussion of the “Scope of work” in section 1.2 briefly outlined the work performed under our DARPA EMIL Phase I work following the original strategies. While all of the research questions addressed and (mostly) answered were essential, one of the most intense area of innovation and new insights came from the work on novel injector regions. Therefore, in chapter 2 of this report, we focus on these innovations. We first present our results on conventional QC lasers, and then discuss a variety of innovative injector region QC lasers, and other innovative QC laser concepts. The sub-sections in this chapter closely follow several publications related to this work. Chapter 3 provides a concise discussion and summary of the results, followed by recommendations for follow-on work.

2. Methods, Procedures and Results

2.1. Conventional design Quantum Cascade lasers

While much of our efforts during this performance period were focused on innovative designs and approaches, we also employed conventional design QC lasers to optimize our efforts on BH growth and processing and laser packaging. Figure 4 below shows the results of one of our best performing conventional devices, which were based on a “two-phonon resonance” design [11]. The highest WPE efficiency measured in CW at 15°C was ~ 6%, which is within the order of magnitude of results reported for similar conventional structures, and the total emitted power reaches 1W under these operating conditions.

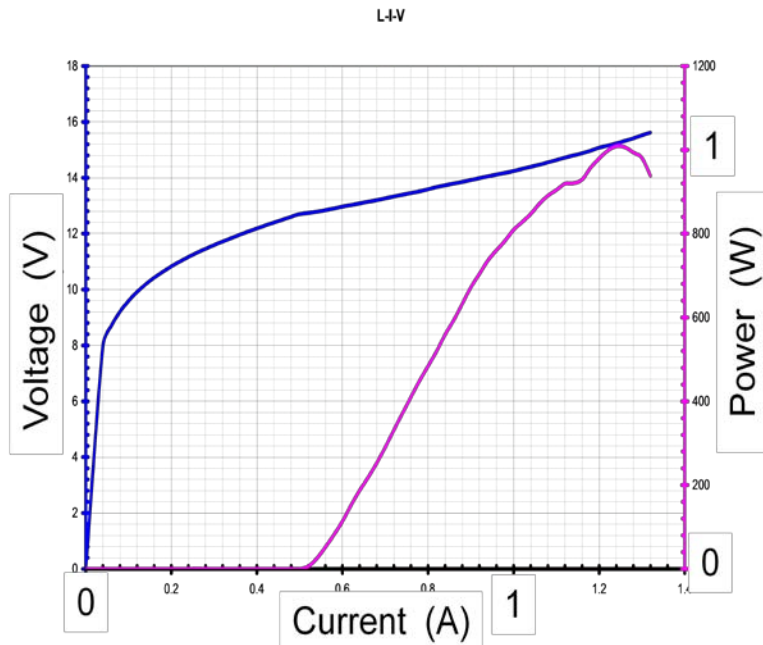


Fig. 4: Light output – current – voltage characteristics of one of our best performing conventional QC lasers. The device was processed as BH laser with a cavity size of 7 μm wide and 5 mm long. The laser was mounted epitaxial-side down. The power refers to the total power of two as-cleaved facets. Heat sink temperature is 15°C. The WPE is 6% at its maximum, and 5.4% at peak output power.

2.2. Low voltage-defect Quantum Cascade laser with heterogeneous injector regions

Strategies to increase the WPE can be separated into two main categories. The first focuses on maximizing the WPE for a given active core design and has been addressed on several fronts, including maximizing the active region gain, reducing the waveguide loss [12, 13, 14], optimizing the outcoupling efficiencies through facet coatings, [15] and improving the thermal management through device geometry, high quality growth, epilayer-side mounting, and BH regrowth[16 – 19]. The second category focuses on improving the quantum design of the active QC laser core. While most of the parameters that maximize the WPE are closely linked with those that maximize output power and result in high performance operation, the design of the active core has yet to take full advantage of the substantial design space. Here, we present a QC laser that adapts the idea of a heterogeneous design and applies it to the injector regions rather than the light generating active regions. For this laser, conventional, doped injectors and novel, undoped injectors with reduced voltage defect are alternated between two different active regions with nominally identical transition energies. The second injector design is used to reduce the voltage drop in the active core that does not contribute to the optical power generated by the laser. For comparison, a conventional QC laser has a voltage defect of approximately 140 meV [17, 20], while the laser reported here has an average voltage defect of less than 79 meV (i.e. about half of the conventional design). The reduced voltage defect injector design in our laser leads to an increase in the WPE of an additional 10 %.

2.2.1. Laser design and fabrication

A portion of the conduction band of the QC laser is shown in Fig. 5. The active core is composed of two optical transitions with identical energies preceded by alternating doped and undoped injector regions. The layer sequence in angstroms of one period starting with the extraction barrier labeled “*” is **25/29/18/24/19/23/21/21/27/20/39/52/13/40/22/33/18/29/19/26/21/21/25/20/27/19/38/13/15/44/13/40/13/34** where $\text{In}_{0.635}\text{Al}_{0.356}\text{As}$ barrier layers are in bold, $\text{In}_{0.678}\text{Ga}_{0.322}\text{As}$ well layers in times roman font, and the n-doped ($4.4 \times 10^{17} \text{ cm}^{-3}$) layers are underlined. The first injector region, labeled A in Fig. 5, is a conventional, doped injector that is optimized for both voltage defect (shaded in green) and electron extraction from the previous transition. The active region following this injector employs a single phonon resonance to empty the lower laser level of electrons; the transition has a design energy of 283 meV. The second injector, B, is undoped and is designed to minimize the voltage defect (shaded in blue) while still providing fast electron extraction. The active region following this injector is a double-phonon resonance design with the same nominal transition energy as the previous active region. A consequence of the low energy drop injector design in this laser is that three states are mixed in the upper-level of the active region following the injector. In conventional designs, typically only two states mix and thus larger than normal broadening of the gain spectrum is expected.

The laser was grown by molecular beam epitaxy (MBE) on low-doped ($n \sim 1 \times 10^{17} \text{ cm}^{-3}$) InP substrate using strain-compensated $\text{Al}_{0.635}\text{In}_{0.365}\text{As}/\text{In}_{0.678}\text{Ga}_{0.322}\text{As}$. The doped injector–first active region–undoped injector–second active region sequence was repeated 17 times and sandwiched between two $0.17 \mu\text{m}$ thick n-doped ($5 \times 10^{16} \text{ cm}^{-3}$) lattice-matched InGaAs layers for enhanced optical waveguide confinement. Additional upper cladding layers of $2.7 \mu\text{m}$ InP

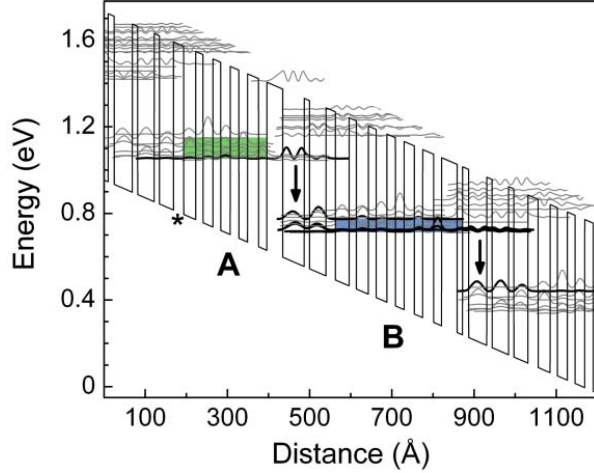


Fig. 5: A portion of the conduction band structure with the moduli squared of the relevant wavefunctions. The optical transitions with design energies of 283 meV are denoted by the vertical black arrows. The doped and undoped injector regions are marked by the letters A and B, respectively. The shaded green and blue regions in the band diagram show the voltage defect for the two injectors. The extraction barrier marked “*”, indicates the first barrier for the design sequence detailed in the main text. The calculation is for an applied electric field of 82 kV/cm.

($1 \times 10^{17} \text{ cm}^{-3}$) and $0.4 \text{ } \mu\text{m}$ InP ($8 \times 10^{18} \text{ cm}^{-3}$) were grown above the top InGaAs layer before a final $100 \text{ } \text{\AA}$ thick layer of InP ($1 \times 10^{19} \text{ cm}^{-3}$). The waveguide has a calculated confinement factor of $\Gamma = 70\%$

The wafer was processed into semicircular mesas for electroluminescence (EL) measurements and into deep-etched ridge waveguide lasers. The mesas were wet etched and $\sim 200 \text{ } \mu\text{m}$ in diameter. The sample was thinned to $\sim 200 \text{ } \mu\text{m}$ and Ti/Au ($250/2500 \text{ } \text{\AA}$) top contacts and Ge/Au ($250/2500 \text{ } \text{\AA}$) back-side contacts were deposited. The mesas were cleaved approximately along the diameter and mounted to a copper heat sink. The ridge waveguide lasers were processed using conventional wet-chemical techniques. The ridge widths varied from 12 to $23 \text{ } \mu\text{m}$, $3300 \text{ } \text{\AA}$ of Si_3N_4 was used for side-wall insulation and Ti/Au ($250/2500 \text{ } \text{\AA}$) was used for top contacts. The InP substrate was thinned to $\sim 200 \text{ } \mu\text{m}$, Ge/Au ($250 \text{ } \text{\AA} / 2500 \text{ } \text{\AA}$) was deposited for back-side contacts, and the lasers were mounted epilayer-up to a copper heat sink with In solder. After the initial characterization, the back facet of several lasers was high-reflection (HR) coated with $\text{SiO}_2/\text{Ti}/\text{Au}/\text{SiO}_2$ ($4000/150/1500/1000 \text{ } \text{\AA}$).

2.2.2. Experimental results and discussion

Pulsed EL measurements were carried out on the cleaved mesas using a Fourier transform infrared (FTIR) spectrometer and a cooled HgCdTe detector. The lasers were mounted to the cold finger of a continuous flow liquid nitrogen cryostat. Pulses of various widths (100 ns to $4 \text{ } \mu\text{s}$) with a 79.9 kHz repetition rate were used. Spectral measurements were recorded from 80 K to room temperature for a large range of applied electric current and are shown in Fig. 6a for 80 K. The inset of the figure shows a current-voltage curve for the device at 80 K. Despite the active core containing two different active region designs, the EL data closely resembles that of a homogeneous design QC laser.

For further inspection, the EL spectra were fit using a nonlinear regression with two Lorentzian functions; a characteristic fit is shown in the inset of Fig. 6b. The spectral position of the peak and the full width at half maximum (FWHM) were determined for each Lorentzian and are shown in Fig. 6b. The two peak positions tune similarly with applied field and are attributed to

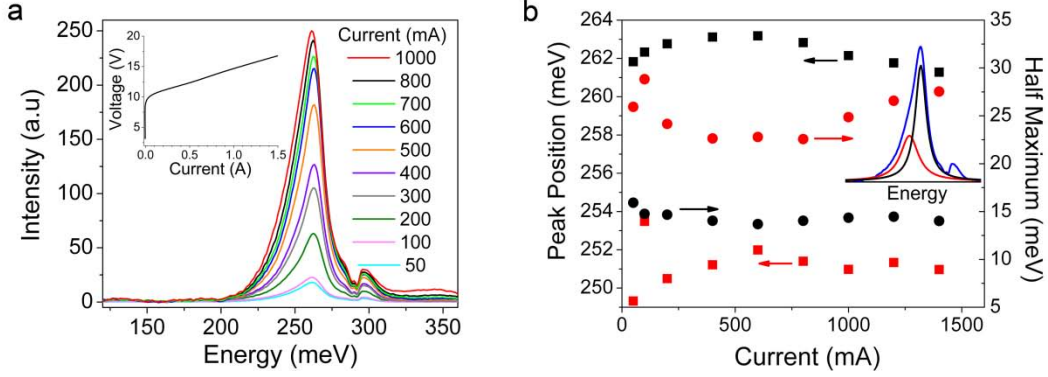


Fig. 6: (a) Pulsed EL spectra at 80 K from cleaved mesas as a function of current. Various pulse widths, 100 ns to 4 μ s, at a repetition rate of 79.9 kHz were used for the measurements. The inset shows a current-voltage plot for the same device at 80 K. (b) Spectral peak position (squares) and full width at half maximum (circles) of the fit Lorentzians versus applied current. The red data points are attributed to optical transitions following the undoped injectors and the black data points are attributed to optical transitions following the conventional injectors. The inset shows a characteristic double-peak Lorentzian fit of an EL spectrum.

the two primary optical transitions shown in Fig. 5. Over the range of applied fields, the spectral positions of the two peaks differ by approximately 10 meV. The higher energy transition (represented by black data points), which we attribute to luminescence from the active region following the doped injector region, has a full width at half maximum around 14 meV and varies by a few percent over the range of applied electric fields. The lower energy luminescence peak (represented by red data) corresponding to light generated from the active region following the undoped injector region has a FWHM that varies by more than 10% and is approximately 10 meV broader than the higher energy peak. The broader transition and the stronger influence of the applied field are attributed to the multiple states that compose the upper-laser level as seen in Fig. 5.

Light-current-voltage (LIV) measurements were performed on many lasers of various ridge widths and cavity lengths. Measurements were performed in pulsed mode operation using 90 ns pulses with a repetition rate of 5 kHz and a room temperature HgCdTe detector. Power measurements were calibrated using a pyrometer detector. A gated integrator and boxcar averager with a 20 ns gate width was used to sample LIV pulses. Figure 7a shows characteristic LI data as a function of temperature for a 1.23 mm long, 15 μ m wide laser. The current-voltage curve for 80 K is also plotted. At 80 K, a peak power of 2.0 W was obtained with a threshold current density of 1.2 kA/cm². The emission wavelength is centered at 4.70 μ m at 80 K and increases to 4.88 μ m at 300 K. The room temperature spectrum of the device at 10 % above threshold current is shown in the inset of Fig. 7a. Using IV data at 80 K for several lasers and assuming the entire voltage drop occurs over the active core, a voltage defect of 79 meV per injector-active region pair is calculated. Allowing for 0.25 V drop due to contact and waveguide resistance [12], a voltage defect of 71 meV per injector-active region pair is extracted. Calculations using the design bandstructure predict a value of 71 meV averaged per injector-active region pair. Threshold current density, J_{th} , as a function of heat sink temperature is plotted

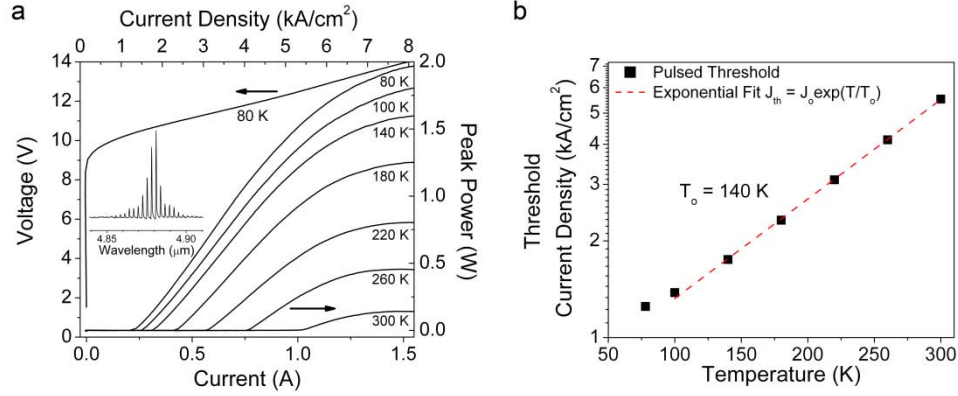


Fig. 7: (a) Light-current measurements for a 15 μm wide, 1.23 mm long laser at different temperatures. The current-voltage curve for the laser at 80 K is also plotted. The inset shows the lasing spectrum of the device at room temperature and 1.1 times the threshold current. (b) Pulsed threshold current density, J_{th} , as a function of the heat sink temperature. The experimental data (squares), excluding 80 K, were fit with an exponential (dashed line), $J_{th} = J_o \exp(T/T_o)$, resulting in $T_o = 140$ K.

in Fig. 7b. The experimental data is fit using an exponential, $J_{th} = J_o \cdot \exp(T/T_o)$, and gives a T_o of 140 K.

Figure 8a shows L-I and η_{wp} -current curves at 80 K for the best performing device with as-cleaved facets and device dimensions of 15 μm x 1.44 mm, where $\eta_{wp} = P/IV$ is the WPE, P is the optical power, I is the current, and V is the voltage. The peak WPE of this laser is 14 % per facet and occurs at a current density, J_{peak} , of 5.6 kA/cm^2 . At this current density, the laser produces a peak power of 2.0 W. The peak WPE, power at J_{peak} , and peak power were also studied as a function of temperature. The results for a 15 μm wide, 1.23 mm long laser are shown in Fig. 8b. The wall-plug efficiency decreases from 12 % at 80 K to 0.7 % at room temperature. The power

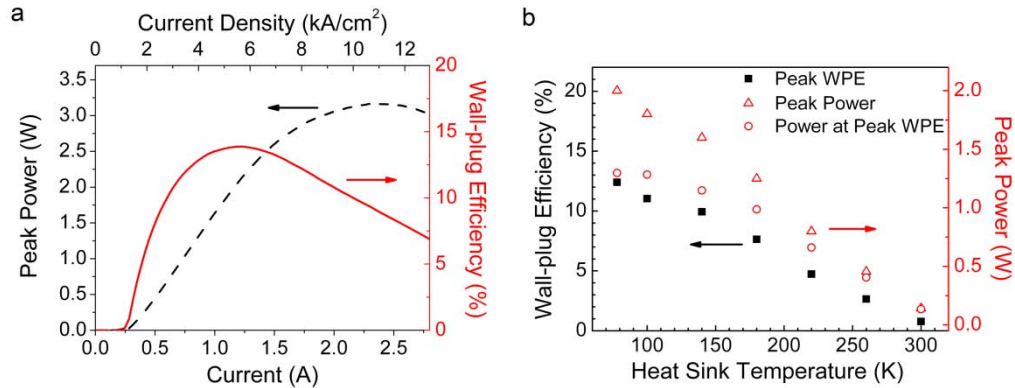


Fig. 8: (a) Peak power (dashed) and wall-plug efficiency (solid) for the best performing, as-cleaved laser (15 μm x 1.44 mm). The device was operated with 90 ns pulses at a repetition rate of 5 kHz. The peak wall-plug efficiency (WPE) occurs at 5.6 kA/cm^2 is 14 % with a power of 2.0 W. (b) Peak WPE (black squares), peak power (red triangles), and power at peak WPE (red circles) as a function of temperature for the laser presented in Fig. 7a.

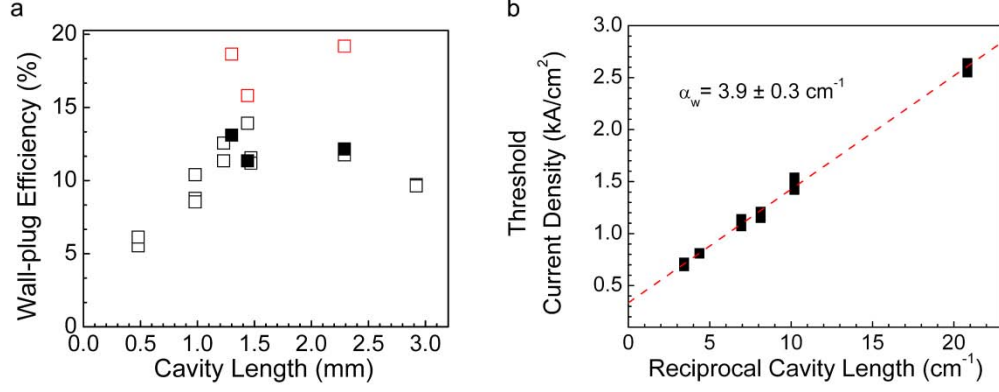


Fig. 9: (a) Pulsed wall-plug efficiency collected from one facet for several lasers versus cavity length. The squares are for uncoated lasers and the red triangles are for select devices that were HR coated on the back facet after initial as-cleaved measurements (black squares). (b) Measured pulsed threshold current density versus reciprocal cavity length at 80 K (filled squares). The dashed line is the result of a linear least squares fit.

at peak wall-plug efficiency is $\sim 60\%$ of the peak device power at roll-over for low temperatures. At higher temperatures, the two power levels converge to approximately the same value. We attribute the strong effect of temperature on both wall-plug efficiency and peak power to insufficient confinement of the upper-laser state in the active region following the undoped injector. Improvements in the design that isolate this state from the continuum should yield better temperature performance.

Figure 9a shows peak pulsed WPE, η_{wp} , as a function of laser cavity length for numerous QC lasers measured at 80 K. The squares represent measurements on uncoated devices, while the red triangles are for select lasers (filled-in black squares) that were high-reflectance (HR) coated on their back facet. For the uncoated lasers, a peak pulsed efficiency of 14 % was measured for a cavity length of 1.44 mm. Likewise for the HR coated lasers, $\eta_{wp} = 19\%$ for a 2.3 mm long laser.

Finally, the waveguide loss of the lasers was estimated by measuring the threshold current density for various cavity lengths at a fixed temperature (80 K). The experimental data is shown in Fig. 9b. Using a linear fit of J_{th} versus the reciprocal cavity length and assuming a facet reflectivity, R , of 0.28, the estimated waveguide loss, α_w , is $3.9 \pm 0.3 \text{ cm}^{-1}$.

2.2.3. Conclusion

In this sub-project we have demonstrated the operation of a strain-compensated $\text{Al}_{0.635}\text{In}_{0.365}\text{As}/\text{In}_{0.678}\text{Ga}_{0.322}\text{As}$ QC laser that employs a new type of a heterogeneous active core. The design consists of interdigitated doped and undoped injector regions between different active regions of nominally identical transition energies. The undoped injectors are designed with reduced voltage defect resulting in an average voltage defect of $\sim 70 \text{ meV}$. Compared to conventional QC lasers this adds another $\sim 10\%$ to the WPE. Laser emission at 80 K is centered at $4.7 \mu\text{m}$ and a peak wall-plug efficiency of 19 % is observed for a 2.3 mm long, $15 \mu\text{m}$ wide

laser with the back facet HR coated. At room temperature, the lasing wavelength is red-shifted to 4.88 μm and η_{wp} decreases to 0.5 %.

2.3. Quantum Cascade lasers with extremely low voltage defect of less than one longitudinal optical phonon energy

With regards to active core design, QC lasers provide a tremendous amount of engineering flexibility which can be exploited to optimize the desired performance characteristics. This sub-project aimed to harness this engineering flexibility to improve the WPE in QC lasers, with particular emphasis on voltage efficiency, which is given as:

$$\eta_v = \frac{E_\gamma n_p}{n_p(E_\gamma + E_\Delta) + qV_s}, \quad (3)$$

where E_γ is the photon energy, n_p is the number of active/injector region periods, E_Δ is the voltage defect per period, and V_s is the parasitic series voltage. The “voltage defect” refers to the energy drop per active/injector period that does not contribute to light generation. As previously outlined, in choosing the voltage defect by design, one must balance two competing factors. A large voltage defect leads to excess energy drop across the structure and wasted voltage over the device. However, a small voltage defect leads to an increase in thermally activated backfilling of electrons from the injector back into the lower laser level of the preceding active region, reducing population inversion.

Here, we focused on maximizing the voltage efficiency by reducing the voltage defect to unprecedented levels. We are able to maintain efficient lower level depopulation and avoid significant thermal backfilling through the use of lower energy states in the active regions that are even lower in energy than the next upper laser level and hence do not contribute to the voltage defect. This allows for a voltage defect that is much smaller than the energy employed for resonant depopulation of the lower laser level. A strategy to further improve voltage efficiency involves reducing V_s , which can be done by rapid thermal annealing the metal contacts [21]. In contrast to previous work featuring low voltage defect QC lasers that use heterogeneous injector regions, as discussed in above section 2.2 and reference [22], here we use a homogenous design to minimize the effect of photon energy mismatch between the differing interleaved structures. We also utilize an injector region of reduced length, consisting of only four quantum wells and barriers, to more rapidly move electrons through the injector into the next upper laser level. This shorter injector results in lower threshold current densities due to the increased gain of more densely packed active transitions, as well as higher maximum current and lower differential resistance due to the shorter injector transit time. Previous work by other groups has focused on injectorless QC lasers [23], including injectorless designs with a low voltage defect, as low as 39 meV [24,25].

2.3.1. Laser design and fabrication

A portion of this design’s conduction band diagram is depicted in Fig. 10. The layer sequence of one period (in angstroms), starting from the first well in the injector, is

25/19/22/21/19/23/18/**30**/13/**11**/41/**13**/37/**16**/32/**22** where $\text{In}_{0.3}\text{Al}_{0.7}\text{As}$ barrier layers are in bold,

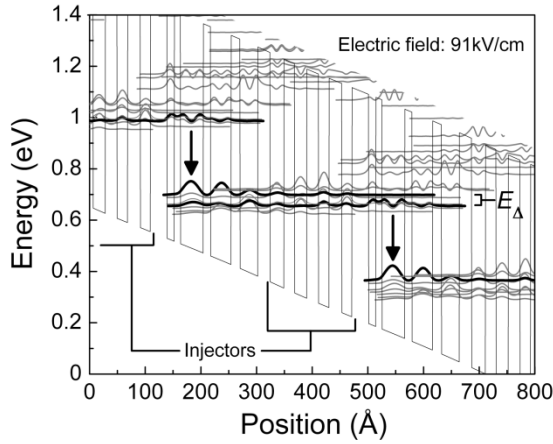


Fig. 10: A portion of the conduction band structure along with the moduli squared of the relevant wavefunctions. Wavefunctions in bold illustrate the upper and lower laser levels of each active period. The optical transition, with a design energy of 298 meV, is depicted by vertical arrows. A very low voltage defect of ~ 36 meV is identified by E_{Δ} , for an applied electric field of 91 kV/cm. One can see the shortened injector regions, consisting of four quantum wells between each set of active regions. The calculation takes the free carrier density into account through a self-consistent solution of the Schrödinger and Poisson equations.

$\text{In}_{0.686}\text{Ga}_{0.314}\text{As}$ well layers are plain, and the n-doped (Si , $1.25 \times 10^{17} \text{ cm}^{-3}$) layers are underlined. The active core is designed for a photon energy of 298 meV, with a voltage defect of 36 meV at turn-on, corresponding to the resonance energy of one longitudinal optical (LO) phonon [26]. This defect is about half that found in conventional QC lasers at turn-on [27] and less than one-third of the voltage defect typically seen under normal operating conditions. Energy states below the lower laser level are spaced one and two phonon resonances lower in energy. The lowest do not contribute to the voltage defect, as there is an upward slope in the injector energy leading to the upper laser level. The injector consists of four pairs of quantum wells/barriers, compared with the seven or eight pairs used in traditional designs of similar photon energy. The total period length is 362 Å, compared with ~ 500 Å in traditional designs [28].

The QC structure was grown by metal-organic chemical vapor deposition (MOCVD) on low-doped ($1 \times 10^{17} \text{ cm}^{-3}$) InP substrate using strain-balanced $\text{In}_{0.686}\text{Ga}_{0.314}\text{As}/\text{Al}_{0.7}\text{In}_{0.3}\text{As}$. High strain (1.1%/1.4%, respectively for InGaAs/AlInAs) was used in the well and barrier material to increase the conduction band offset and allow for high photon energy while still isolating the upper laser level from the continuum. The total structure consists of a low-loss InP waveguide (doped mostly at $n \sim 2 \times 10^{16} \text{ cm}^{-3}$) surrounding 41 periods of injector/active region. Devices were fabricated as deep-etched ridge waveguide lasers of varying widths with SiO_2 (3000 Å) for side-wall electrical insulation. The devices were thinned to $\sim 200 \mu\text{m}$ and Ti/Au (200 Å/6000 Å) top contacts and Ge/Au (200 Å/3000 Å) bottom contacts were deposited. Ridges were cleaved to various lengths between 0.5 and 3.9 mm and mounted epitaxial-side up on copper heat sinks. For CW measurements, a set of devices was fabricated with electroplated gold top contacts for improved thermal conductivity. These devices were deep-etched in a double-trench configuration, again using SiO_2 for side-wall electrical insulation, with 8 μm of electroplated gold on the top contact, and similar processing for the remainder of the structure.

2.3.2. Experimental results and discussion

Voltage efficiency and voltage defect are experimentally determined according to Eq. 3, where the denominator is equivalent to the total voltage drop across the structure. The photon energy was measured at various temperatures (see inset of Fig. 13). The parasitic series voltage, V_s ,

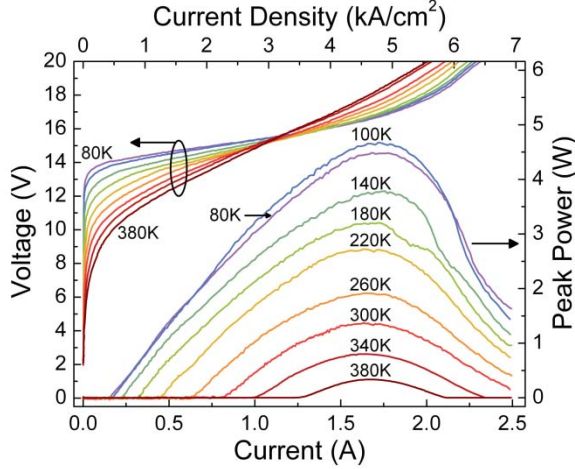


Fig. 11: Pulsed LIV measurements for a 3 mm long and 12 μm wide laser ridge at the indicated heat-sink temperatures. The light, showing output from both facets, is corrected for a collection efficiency of 75%.

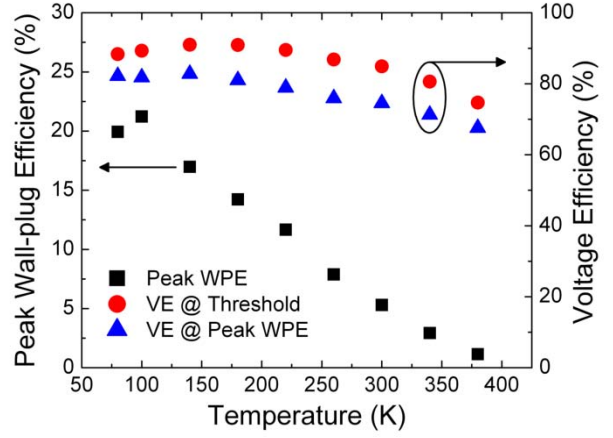


Fig. 12: Peak WPE (squares), voltage efficiency at lasing threshold (circles), and voltage efficiency at peak WPE (triangles) versus heat-sink temperature for a 3 mm long and 12 μm wide laser ridge under pulsed operation.

refers to all of the voltage drop in the structure not occurring in the active core and includes effects such as contact and wiring resistance. This parasitic voltage ranged from 0.4 V at low temperatures to 0.55 V at room temperature and was experimentally found through current-voltage measurements performed on a QC laser structure without an active core [21]. Pulsed light-current-voltage (LIV) measurements were performed on devices of different lengths at several heat-sink temperatures. Fig. 11 shows results for a representative 3 mm long and 12 μm wide ridge. This device had a low pulsed threshold current density at 80 K of 440 A/cm², with a coincident voltage defect of only 30 meV. The voltage defect fell to less than 20 meV at 180 K. This exceptionally low value for the voltage defect is clearly below the energy of an LO-phonon (~ 34 meV in this material system [26]), the conventional scattering mechanism for depopulation of the lower laser level in QC lasers. A voltage defect with energy corresponding to at least one LO-phonon for lower laser level depopulation is generally considered essential for QC laser operation; usually two or more LO-phonons are employed. Here we see that a voltage defect of much less than one LO-phonon can still provide good overall laser performance.

As an indicator of performance, the WPE was measured. At 100 K, the peak WPE for a 3 mm long cavity was 21%, with a voltage defect at this peak efficiency point of 54 meV. This corresponds to values of 89% and 82% for the voltage efficiency at the threshold and peak WPE operating points, respectively. Analogous values at room temperature are 5.3% for peak WPE, 85% for voltage efficiency at threshold, and 75% for voltage efficiency at the peak WPE operating point. One can see the progression of the peak WPE, threshold voltage efficiency, and voltage efficiency at peak WPE with temperature in Fig. 13. Voltage efficiency reached as high as 91% at threshold for 180 K. The increase in voltage efficiency from low temperatures to intermediate temperatures is a result of the lowering of the voltage turn-on due to increased thermal energy of electrons moving through the structure; the subsequent drop in voltage efficiency at even higher temperatures is a consequence of exponentially rising threshold

currents resulting in higher threshold voltages. To gauge CW performance, LIV measurements were performed on lasers with thick electroplated gold top contacts mounted epitaxial-side up on a copper block. At 80 K, peak CW WPE was 19%, with voltage efficiency at threshold and peak efficiency of 82% and 76%, respectively. This performance is similar to that seen in pulsed operation at the same temperature.

By measuring 80 K pulsed threshold current density versus cavity length, a waveguide loss (α_m) of 1.7 cm^{-1} was determined. Ridge widths ranging from 10 to $14 \text{ }\mu\text{m}$ were used, with no major variability in threshold current density with width. Waveguide loss was found to increase with higher temperature, as previously reported for longer wavelength QC lasers [29]. Considering the high voltage efficiency, low waveguide loss, and low threshold currents in these devices, one would expect even higher WPE. However, the sub-phonon voltage defect results in relatively long injector transit times, reduced slope efficiency, and subsequently diminished wall-plug efficiency. The shorter length of the injector does not compensate for this effect, as other factors dominate, such as the upward slope of injector ground state energies from one active region to the next (see Fig. 10), which leads to a pooling of electrons in the lowest energy state of the active region. Another factor reducing injector transit time is the long tunneling time for the thick injection barrier [30].

Figure 13 shows the temperature performance of the laser; the characteristic temperature T_0 is around 118 K at lower temperatures and 174 K at higher temperatures. One would expect much lower T_0 values due to considerable thermal backfilling of the lower laser level because of the low voltage defect. However, the energy levels in the active region below the lower laser level help compensate for this effect. Thus the effective voltage defect can be as low as 20 meV while still allowing the lower laser level to depopulate through LO-phonon scattering. Still, the rise in threshold current with temperature has a distinct slowdown once the voltage defect at threshold reaches the energy of an LO-phonon (see Fig. 13). This highlights the importance of a voltage defect with energy corresponding to at least one LO-phonon resonance for good high temperature performance.

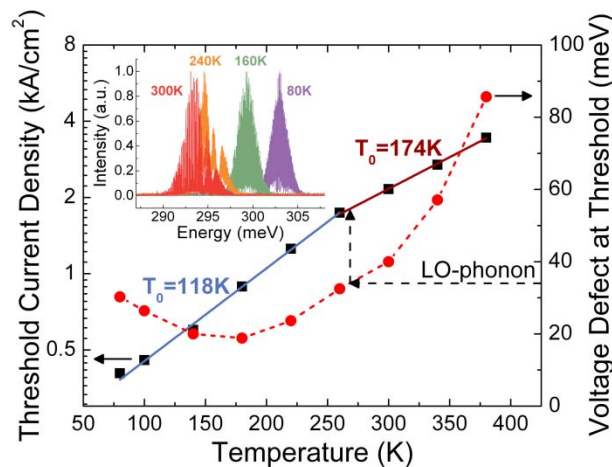


Fig. 13: Threshold current density (black squares) and voltage defect at laser threshold (red circles) versus heat-sink temperature for a 3 mm long and $12 \text{ }\mu\text{m}$ wide laser ridge under pulsed operation. The threshold current density values are fit with exponential curves, $J_{th} = J_0 \exp(T/T_0)$, resulting in two regions of differing characteristic temperature T_0 . A T_0 of 118 K exists at lower temperatures, while a T_0 of 174 K is obtained at higher temperatures. The discontinuity in the temperature performance occurs where the voltage defect at threshold corresponds to one LO-phonon ($\sim 34 \text{ meV}$). The inset shows pulsed laser spectra for the device at 1.1 times threshold for various heat-sink temperatures.

2.3.3. Conclusions

In conclusion, we demonstrated a QC laser design approach that produces the highest reported voltage efficiency for any QC laser. This device features a short, four-quantum-well injector with an ultra-low voltage defect (less than 20 meV), well below the energy of one LO-phonon. This low voltage defect, combined with high photon energy, results in a low and room temperature voltage efficiency of 82% and 75%, respectively, at the peak WPE current. A voltage efficiency as high as 91% is exhibited near threshold for intermediate temperatures. Furthermore, low threshold current densities and low waveguide loss show promise for improved overall performance.

2.4. Quantum Cascade lasers with ultra-short injector regions

2.4.1. Introduction

Most high performance QC lasers before the work conducted under the DARPA EMIL program were based on design advances made before or around 2001, [31-33]. Since that time, no significant improvement had been realized by implementing a fundamentally different QC design. The 2001 design advance [33] that led to the first CW RT QC laser [34] is the so-called “double-phonon” structure. The double-phonon active region is composed of at least three wells, where each of the three lowest coupled active region quantum ground states are spaced one longitudinal optical (LO) phonon energy apart; this allows enhanced relaxation out of the lower laser state [34].

While much attention has been paid to improving QC performance by incremental modifications to this *active region* structure, we here focused on a re-examination of the role of *injector regions* in QC laser performance. Since injector regions themselves are not the source of photon generation, prior work in the field has examined the possibility of eliminating injector regions altogether. In these “injectorless” QC structures, active regions are successively stitched together without the aid of injector region energy states. [35-37]. In conventional QC structures, the injector regions do, however, serve a multitude of important functions:

- efficient injection of electrons into the upper laser state;
- isolation of the upper laser state from the continuum;
- Bragg reflection of the upper laser state, preventing electron escape by tunneling;
- facilitation of electrons in “relaxing” out of the active region;
- spatial and energetic separation of the lower laser state from the downstream electron pool;
- providing space over which electrons can gain energy relative to the conduction band edge; and
- providing a convenient space for doping to reduce impurity scattering.

Given the many important functions of QC injector regions, in this sub-project, we examined QC structures with highly minimalized injector regions. Conventional mid-infrared QC laser designs typically have between five and nine injector wells (shorter wavelength designs generally employ more injector wells). Here, we study short-wavelength ($\lambda < 5 \mu\text{m}$) QC designs that have either two or three injector wells.

Key among the performance parameters of high quality lasers are small threshold current densities, large slope efficiencies, and large wall-plug efficiencies. In examining the relations for each of these performance parameters, we see that injector length plays a key role. For example,

the low temperature threshold current density contains the total thickness of the active core through via the length of one active region, the number of stages, and the optical confinement factor. For any fixed value of active core thickness and waveguide configuration, lower thresholds are achieved when more QC periods are squeezed into the QC stack. Ideally then, one should shorten the overall QC period length. But the length of the QC active region is somewhat fixed for any given emission wavelength and active region design strategy. The only practical place to decrease the QC period length is the injector region.

However, when considering short injector QC structures, one must be mindful that shortening the injector regions can potentially lead to the deleterious effect of decreased upper laser state injection efficiency. This may occur, for example, via more readily populating the active region state immediately above the upper laser state, out of which electrons can easily scatter (non-radiatively) to energy states below the upper laser state. As injector lengths are shortened and more QC periods are added to the active core, we can likewise expect an increase in total output power. Shortened injectors reduce the threshold current density, which is accompanied by a commensurate increase in output power. As a result, the wall-plug efficiency (Eq. 1) rises accordingly.

Finally, shorter injection regions also lead to a delayed roll-over, as the maximum current density for a given – and ideally very low – doping level is inversely dependent on the carrier transit time through the QC stages. A shorter injector offers the opportunity for faster transit times, hence higher current densities. [38, 39]

When designing short injector QC lasers, one becomes particularly aware of the operating field. For a fixed emission wavelength, the operating field and period length are about inversely proportional. The consequential higher operating field for shortened injector regions often results in more difficulty in designing confinement for the upper laser state which can be counteracted by use of high band-offset strained materials and sometimes leads to laser reliability problems.

Given the evident advantages and minor caveats as out lined above, we set out to design short-wavelength QC lasers with shortened injector regions, especially injection regions with 3 and 2 quantum wells.

2.4.2. Quantum Cascade laser with three injector wells

2.4.2.1. Design and fabrication

We designed a QC laser consisting of six quantum wells per QC period – shown in the Figs. 14 and 15 conduction band diagram – with photon energy 239 meV ($\lambda = 5.19 \mu\text{m}$) and energy defect 116 meV. With three active region wells and three injector wells, the total period length was 307 Å in contrast to $> 500 \text{ Å}$ for the best conventional QC structures [31]. The combination of energies and period length result in a turn-on field of 114 kV/cm. The layer sequence is, in angstroms starting from the injection barrier, **32** / 52 / **10.5** / 43 / **8.5** / 36 / **16** / 27 / 16.5 / 26 / 18 / 21.5, where $\text{Al}_{0.710}\text{In}_{0.290}\text{As}$ layers are in bold type, $\text{In}_{0.638}\text{Ga}_{0.362}\text{As}$ layers are in plain type, and layers Si-doped $n = 1.0 \times 10^{17} \text{ cm}^{-3}$ are underlined; the structure has an active core sheet density $n_s =$

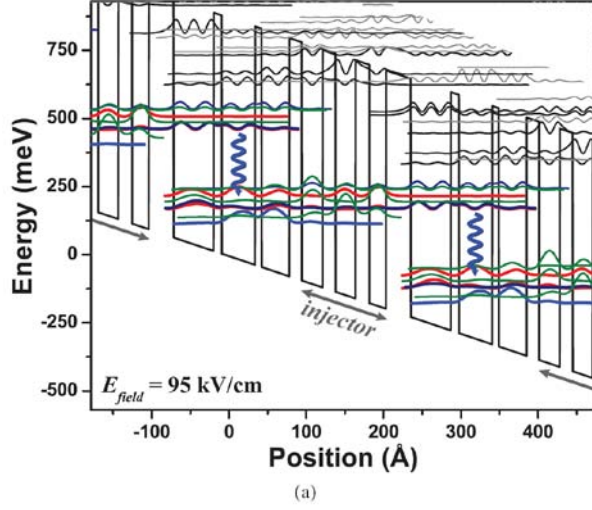


Fig. 14: QC structure with three injector wells and three active region wells. At 95 kV/cm the second energy level of one active region is in resonance with the down-stream upper laser state at this field.

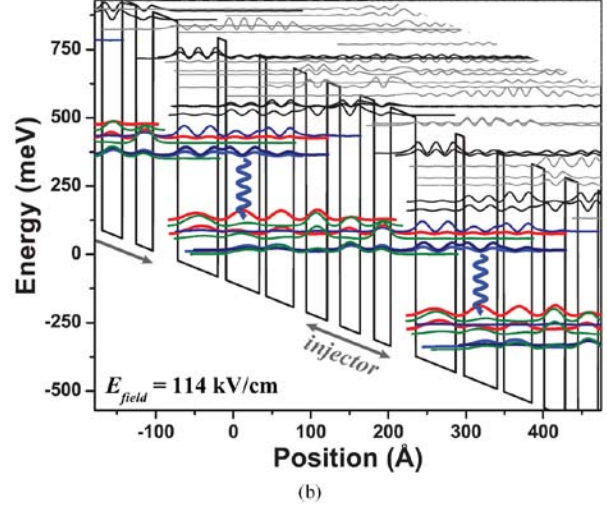


Fig. 15: QC structure with three injector wells and three active region wells. The as-designed turn-on field is 114 kV/cm.

$1.1 \times 10^{11} \text{ cm}^{-2}$ per period. At 125 kV/cm, where the upper and lower laser states are somewhat isolated, we calculate $\tau_u = 1.4 \text{ ps}$, $\tau_l = 0.5 \text{ ps}$, $\tau_{ul} = 5.6 \text{ ps}$, and $z_{ul} = 20.6 \text{ Å}$.

The laser was grown using metal-organic vapor phase epitaxy (MOVPE) on a low doped ($n < 2 \times 10^{17} \text{ cm}^{-3}$) InP substrate. The QC active–injector sequence was repeated 50 times. The QC active core was surrounded on each side by 0.12 μm $\text{In}_{0.53}\text{Ga}_{0.47}\text{As}$ Si-doped $n = 0.5 \times 10^{17} \text{ cm}^{-3}$ to enhance gain region confinement factor. Following the $\text{In}_{0.53}\text{Ga}_{0.47}\text{As}$ confinement layer, the top cladding consisted of 2.5 μm InP Si-doped $n = 0.5 \times 10^{17} \text{ cm}^{-3}$, 0.7 μm InP Si-doped $n = 80 \times 10^{17} \text{ cm}^{-3}$, 0.1 μm InP Si-doped $n = 200 \times 10^{17} \text{ cm}^{-3}$, and finally 0.06 μm $\text{In}_{0.53}\text{Ga}_{0.47}\text{As}$ Si-doped $n = 500 \times 10^{17} \text{ cm}^{-3}$. Standard quantum well gradings between bulk $\text{In}_{0.53}\text{Ga}_{0.47}\text{As}$ and InP regions were used to assist electron transport across the bulk interfaces.

Ridge lasers with thin Au top contacts were fabricated using standard processes [40]; BH devices with InP overgrowth were likewise fabricated. We also fabricated and tested electroluminescence (EL) mesas [40] designed to suppress optical feedback in order to study spontaneous emission properties of the structure.

2.4.2.2. Results and discussion

We examined the light–current–voltage (LIV) properties of both EL mesas and ridge lasers. We observe a pronounced negative differential resistance (NDR) feature in all devices. In EL mesas at a heat sink temperature $T_{\text{sink}} = 80 \text{ K}$ and current densities near 0.3 kA/cm^2 , we see a rapid 1.7 V (11 kV/cm) “jump,” as shown in Fig. 16a. The voltage increase is accompanied by a reduction in current density of 0.13 kA/cm^2 . After the NDR feature, the differential resistance decreases by a factor of 2. We also observe in the LI data that, after the NDR feature, the radiative efficiency increases by a factor of 3. We furthermore see from Fig. 16b that the NDR persists through room temperature. The NDR can be understood in that the two operating states—before the NDR feature and after—represent two different energy band configurations.

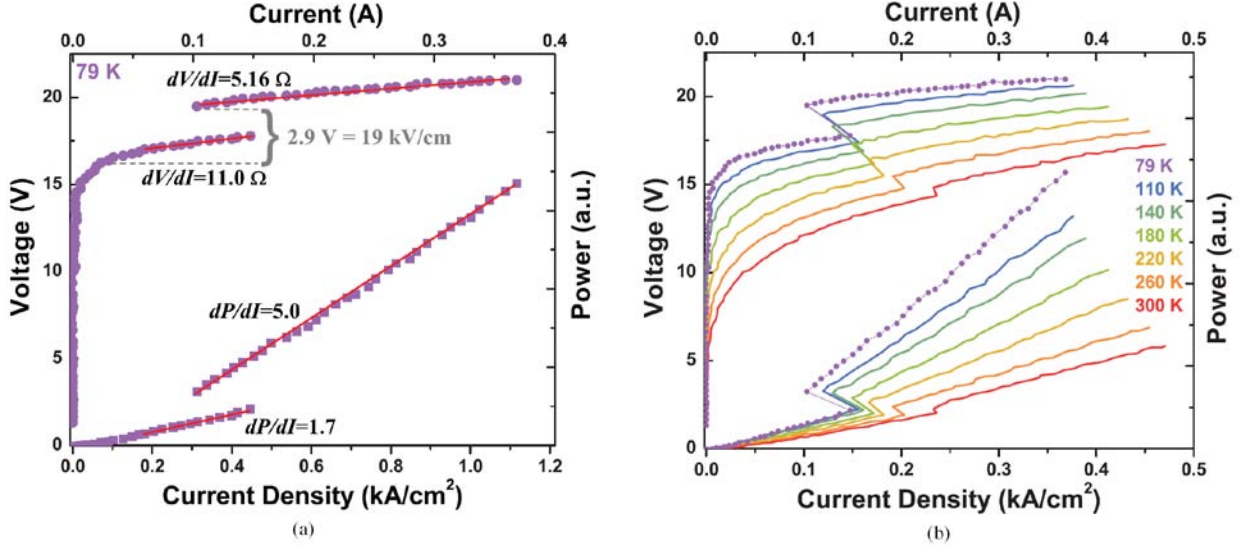


Fig. 16: Pulsed light-current-voltage (LIV) data of electroluminescence mesas for the three injector well QC structure. The area of the tested device is 0.033 mm^2 . Pronounced negative differential resistance is seen at low temperature (a) and persists through room temperature (b).

At $T_{\text{sink}} = 80 \text{ K}$, the difference in turn-on of the two current paths is 2.9 V (19 kV/cm). Associating the current path in operation after the NDR feature with the band alignment at the design field of 114 kV/cm , the first current path operates with turn-on at 95 kV/cm . The energy diagram at 95 kV/cm , plotted in Fig. 14a, elucidates a process of electron transport across the injector region after just a single phonon transition from the lower laser state. In this case, the voltage defect is $\Delta = 49 \text{ meV}$, rather than the 116 meV at 114 kV/cm . Interestingly, this is strong evidence of current flow and light generation with the lowest state of one active region significantly below the upper laser state of the next downstream active region. At the lower field of 95 kV/cm in Fig. 14, most of the dopant electrons are “trapped” in the lowest active region state.

Electroluminescence spectra collected at pre- and post-NDR points lack any discernable spectral changes between the two operating points. We thus conclude that the upper and lower energy states of the optical transition remain the same between the two operating points. The field re-alignment changes only the configuration of the injector states relative to the active region states.

The data become all the more interesting for laser devices, *i.e.* with the inclusion of stimulated emission in the overall device behavior. Figure 17a shows that no NDR is observed in the current-voltage (IV) data at 80 K . Rather, the NDR only appears at temperatures near and above 140 K . Figure 17b shows the onset of NDR behavior with greater temperature resolution. Here, we see the NDR feature appear at 130 K , the first temperature where threshold current density is greater than the current density at which the NDR occurs ($J_{\text{th}} > J_{\text{NDR}}$). Apparently, it is the presence of cavity photons (stimulated emission) that prevents the observation of NDR and locks the laser into the pre-NDR band configuration for $T_{\text{sink}} < 130 \text{ K}$. Also of note is that the laser exhibits two thresholds for $T_{\text{sink}} = 130 \text{ K}$ and slightly above. The two thresholds directly result from the NDR—that is, the decrease in pumping current as the energy level configuration re-aligns at the higher field. Perhaps even more surprising, for T_{sink} corresponding to $J_{\text{th}} > J_{\text{NDR}}$,

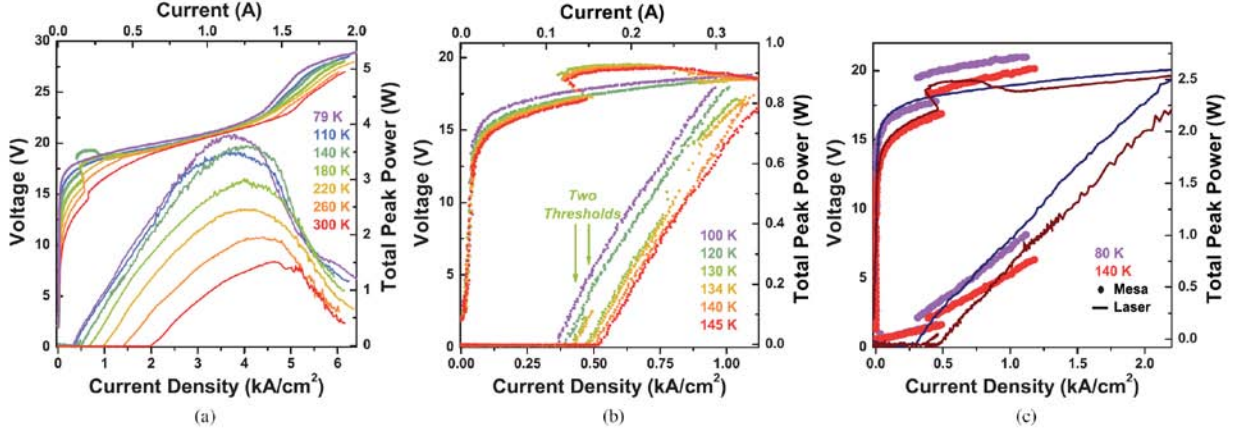


Fig. 17: Light-current-voltage (LIV) data for a representative three injector well $10.4 \mu\text{m} \times 3 \text{ mm}$ ridge laser device. As seen in (a), negative differential resistance (NDR) is observed, but only at elevated temperatures. From (b), we see that the NDR appears only for $J_{th} > J_{NDR}$, i.e. here for $T_{sink} \geq 130 \text{ K}$. Because of the NDR, we observe two thresholds for $T_{sink} = 130 \text{ K}$ and slightly above. The comparison of LIV data from this laser device and EL data from Fig. 16b, as in (c), shows the effect of cavity photon density on the current-voltage behavior.

increasing cavity photon density actively “pulls down” the operating voltage, effectively to the internal the pre-NDR state. This, in fact, is a second form of NDR, where voltage decreases with increasing current, rather than the more typically thought-of NDR where current decreases with increasing voltage. The feature can plainly be seen in Fig. 17c, where we compare LIV data from mesa and laser devices at $T_{sink} = 80 \text{ K}$ and 140 K .

The behavior of these two NDR features for laser devices can be explained by considering contributions to the total per period transport rate. We can simplify the total carrier transit time through a QC period as being the sum of active region and injector region transit times due to non-radiative processes such as phonon scattering, and including a term that accounts for photon-assisted transport due to stimulated emission. The stimulated emission term effectively decreases the active region transit time.

To explain the first NDR feature, where the temperature dependence of J_{th} affects the presence of this NDR, we return to our consideration of J_{max} . Stimulated emission significantly extends J_{max} , especially if the total non-radiative transport time is dominated by τ_{act} (due to the long lifetime of the upper laser state) in the absence of stimulated emission. Thus, for temperatures below 130 K where no NDR is observed, $J_{max}(E_{field} = 95 \text{ kV/cm})$ includes stimulated emission and is therefore large. For temperatures at and above 130 K where we see NDR, $J_{max}(E_{field} = 95 \text{ kV/cm})$ is smaller since $J_{th} < J_{max}$. To explain the second NDR feature, where voltage decreases with increasing current for $T_{sink} \geq 130 \text{ K}$, we again look to the effect of stimulated emission on the transit time and maximum current density. Specifically, this behavior can be understood with the insight that J_{max} changes with the presence of stimulated emission. The dynamic shift of J_{max} results in the laser facing the option of two transport paths. For $T_{sink} \geq 130 \text{ K}$, J_{max} at $E_{field} = 114 \text{ kV/cm}$ is greater than J_{th} , but *once lasing has been established* due to the presence of stimulated emission, J_{max} at $E_{field} = 95 \text{ kV/cm}$ is *also* greater than J_{th} . Now, with two available transport paths, the laser selects the path that leads to minimum operating power (and here, lower operating voltage).

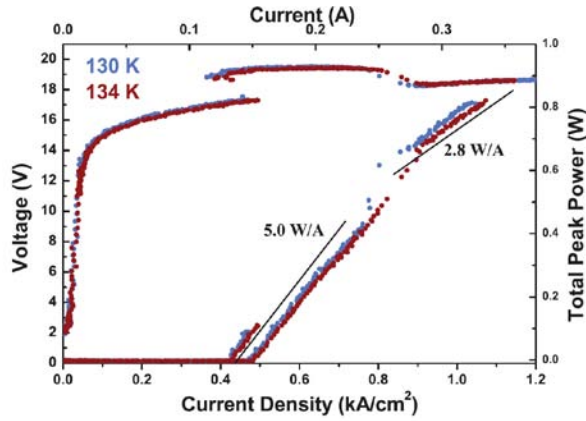


Fig. 18: LIV data near the transition $J_{th} > J_{NDR}$, here for $T_{sink} = 130$ and 134 K. Different slope efficiencies are observed before and after the band configuration that results from the presence of stimulated emission. No significant change in slope efficiency is observed before and after the NDR point.

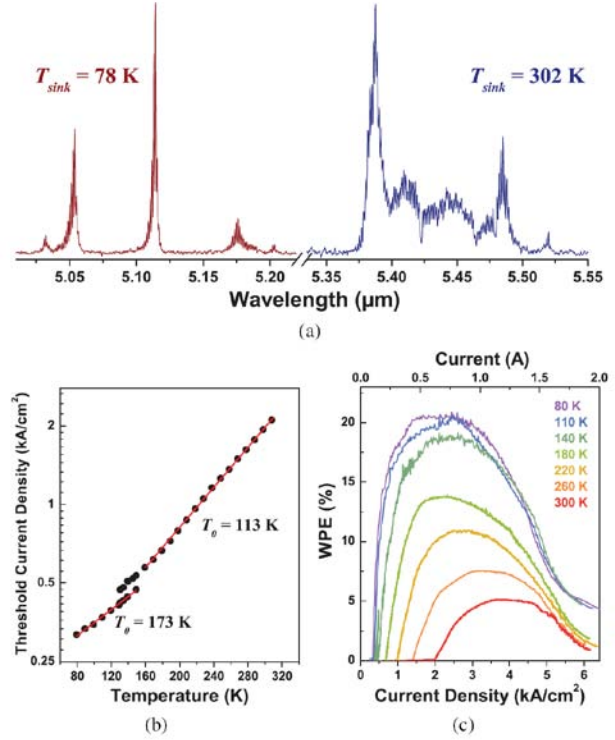


Fig. 19: (a) Representative normalized spectra of the three injector well structure for $T_{sink} = 78$ K and 302 K near threshold. Characteristic temperature T_0 (b) and pulsed wall-plug efficiency (c) for a $10.4 \mu\text{m} \times 3 \text{ mm}$ ridge laser device.

Thus, the presence of stimulated emission causes the laser to revert back to the lower field configuration. After the second NDR feature, we observe a marked decrease in slope efficiency. In Fig. 18, we see that the slope efficiency for the low field band configuration (Fig. 15a) is nearly half that of the high field configuration (Fig. 15b): 2.8 vs. 5.0 W/A, respectively. This discrepancy is at least consistent with the factor of 3 observed in the EL case (Fig. 16).

2.4.2.3. Device performance

Lasing occurs at $\lambda \sim 5.1 \mu\text{m}$ for $T_{sink} = 79$ K and at $\lambda \sim 5.4 \mu\text{m}$ at room temperature, as shown in Fig. 19a. For the ridge laser device described by the Fig. 17 data, pulsed total output power peaks at 3.8 W at 80 K, while room temperature output power is 1.5 W. Threshold current density is as low as 313 A/cm^2 at 80 K, and reaches 2.0 kA/cm^2 at room temperature. Figure 19b explains this increase, with the rather low characteristic temperature $T_0 = 113$ K for T_{sink} where $J_{th} > J_{NDR}$. However, for T_{sink} where $J_{th} < J_{NDR}$, T_0 is much higher at 173 K. Wall-plug efficiency—as shown in Fig. 19c—peaks at 20.5% for $T_{sink} = 80$ K and 5.1% at 300 K.

2.4.3. Quantum Cascade laser with two injector wells

2.4.3.1. Design and fabrication

To further test such short injector structures, we designed a second laser with only two injector wells and three active region wells. Besides the removal of one injector well, the two laser designs are otherwise similar. The photon energy was designed to be 241 meV ($\lambda = 5.14 \mu\text{m}$) and the energy defect was designed to be 116 meV. The total QC period length was 274.5 \AA , for a design field $E_{field} = 128 \text{ kV/cm}$.

As shown in the Fig. 20 conduction band diagram, the layer sequence is, in angstroms starting from the injection barrier, **35** / 53 / **10.5** / 43 / **8.5** / 35 / **21** / 28.5 / 15.5 / 24.5, where $\text{Al}_{0.710}\text{In}_{0.290}\text{As}$ layers are in bold type, $\text{In}_{0.638}\text{Ga}_{0.362}\text{As}$ layers are in plain type, and layers Si-doped $n = 1.4 \times 10^{17} \text{ cm}^{-3}$ are underlined; the structure has an active core sheet density $n_s = 0.96 \times 10^{11} \text{ cm}^{-2}$ per period. At 132 kV/cm, where the upper and lower laser states are somewhat isolated, we calculate $\tau_u = 1.4 \text{ ps}$, $\tau_l = 0.2 \text{ ps}$, $\tau_{ul} = 4.6 \text{ ps}$, and $z_{ul} = 20.1 \text{ \AA}$. The laser was grown by MOVPE with a waveguide structure identical to that described in the previous section. Fabrication and processing were also similar.

2.4.3.2. Results and discussion

Similar to the three well injector design reported in the previous section, LIV data for this design also show NDR; in this case though, it is much less pronounced. Following the analysis of the previous section, the NDR appears 3.6 V (26 kV/cm) below the designed turn-on voltage. In this design, we calculate that the upper laser state and the second active region state of the up-stream active region mix at $E_{field} = 103 \text{ kV/cm}$; here, the difference—25 kV/cm—between the field at which these states align and the designed turn-on field is in excellent agreement with the data. However, the states mix to a much less extent, which is consistent with the lower current change associated with the NDR feature.

The two injector well design shows other characteristic features in the LIV data. For example, in Fig. 21 we see two physically separate mechanisms that limit light output. For an applied 20 V, we see an increase in differential resistance; the feature is roughly independent of temperature, and it corresponds to a drop in slope efficiency. A second increase in differential resistance is observed, this time at a constant current density of about 7 kA/cm^2 (independent of temperature). Again, this feature generally corresponds to a decrease in output power. That the first effect appears with constant applied field and the second appears with constant current density is telling of the physical origins. The constant current feature is the “turn-off” most commonly seen in QC lasers, where a maximum current density is reached based on the intrinsic transit times and the finite amount of doping n_s of the QC structure [39].

The constant-voltage turn-off feature in Fig. 21 is not as commonly observed. One explanation for this feature arises from examining the injector region configuration relative to the active region at different fields. At $T_{sink} = 79 \text{ K}$, the difference between the turn-on voltage of the device and this constant-voltage turn-off is about 2.1 V (15 kV/cm). Our laser was intentionally designed for the lowest state of one active region to be in resonance with the upper laser state of the adjacent down-stream active region at threshold, providing efficient transport between active regions and thus decreasing τ_{inj} . In this design, these levels are in full resonance when $E_{field} = 128 \text{ kV/cm}$. However, because of the spatial separation of these two states, they remain strongly

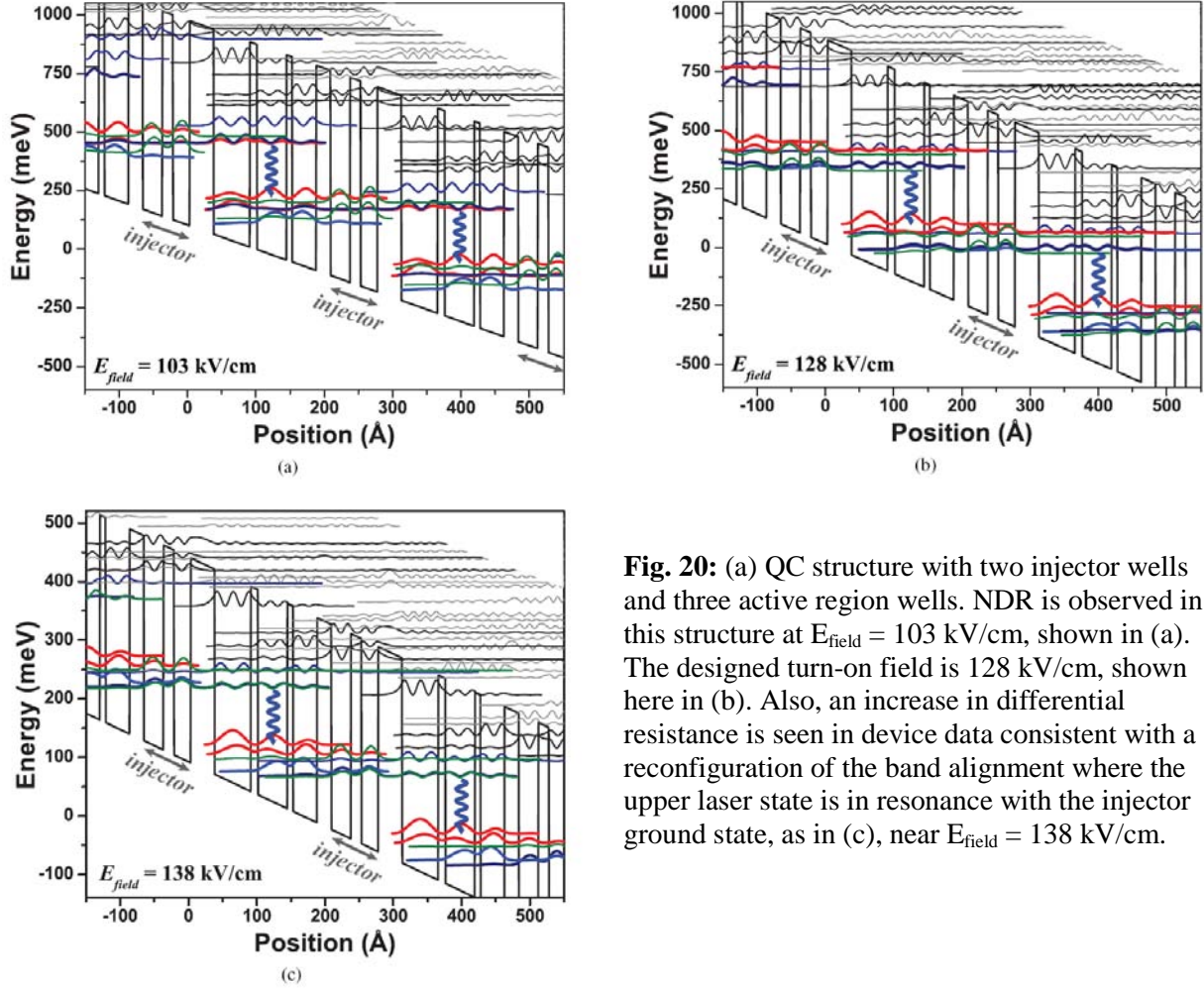


Fig. 20: (a) QC structure with two injector wells and three active region wells. NDR is observed in this structure at $E_{\text{field}} = 103 \text{ kV/cm}$, shown in (a). The designed turn-on field is 128 kV/cm , shown here in (b). Also, an increase in differential resistance is seen in device data consistent with a reconfiguration of the band alignment where the upper laser state is in resonance with the injector ground state, as in (c), near $E_{\text{field}} = 138 \text{ kV/cm}$.

coupled over only a small field range. At $E_{\text{field}} = 128 \text{ kV/cm}$, the lowest injector state is below these two aligned states; increasing the field to 138 kV/cm puts the lowest injector state and the upper laser state in full resonance. This secondary field alignment and electron path is conceivably slower, as electrons have to travel through an additional state, increasing the differential resistance. The increase in differential resistance observed at constant applied field with variations in temperature may thus arise from these two injector region alignments. The successful operation of both these band alignments is further evidence that electrons can *directly* tunnel from one active region to the next in these short injector structures.

Yet another interesting feature is seen in the Fig. 21 LIV characteristics. Rather than peak output at the lowest temperatures, these lasers have peak output at elevated temperatures (180 K in this device), while highly unstable pulse behavior at lower temperatures limits average output power. The time evolution of the light pulse over the 100 ns period also indicates highly irregular behavior, with pulse-to-pulse variations on the order of 100 mW at low temperatures. These pulse instabilities are damped with increasing temperature, and they disappear around 140 K .

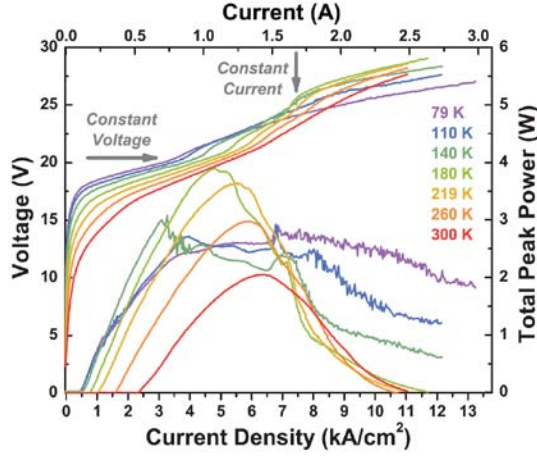


Fig. 21: Pulsed LIV data for a representative two injector well $7.5 \mu\text{m} \times 3 \text{ mm}$ BH laser device. Two “turn-off” features are seen, one occurring with constant voltage and one with constant current. Pulse instabilities in the light power are also evident at lower temperatures. Because of these instabilities, output power is highest at elevated temperatures. The data shown here are for sampling averaged over ~ 15 pulses.

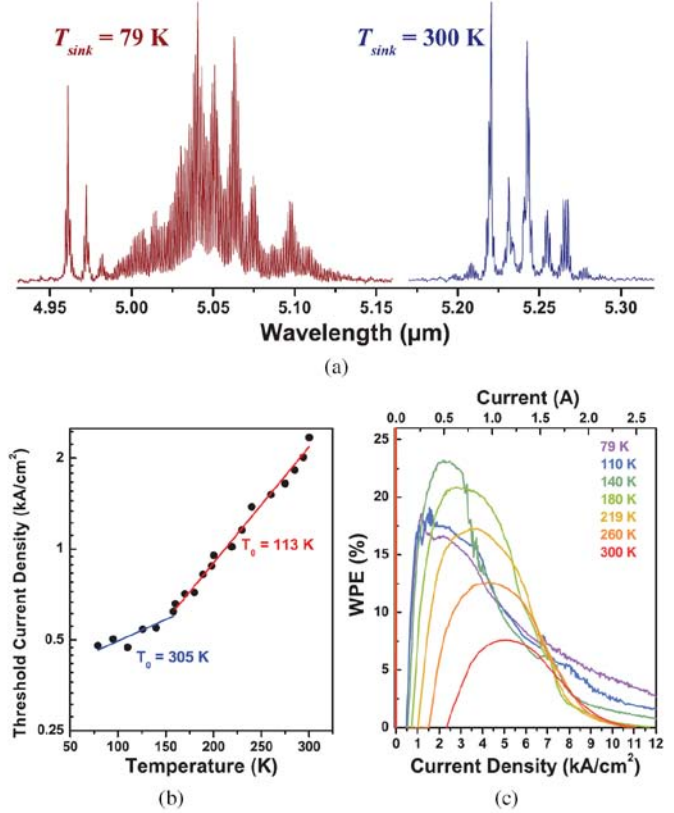


Fig. 22: (a) Representative normalized spectra of the two injector well structure for $T_{\text{sink}} = 79 \text{ K}$ and 300 K near threshold. Characteristic temperature T_0 (b) and pulsed wall-plug efficiency (c) for a two injector well $7.5 \mu\text{m} \times 3 \text{ mm}$ BH laser device.

In QC structures, electric field profiles are largely assumed to be homogenous when the doping density is low, or periodic but stable when the doping density is higher. However, charge instabilities have long been known to exist in superlattice structures [41]. Intuitively, charge instabilities can result when local disruptions of the charge density locally perturb the field, leading to electric field domains. The highly nonlinear event of lasing onset is expected to exacerbate this instability, and in these minimalized QC structures, these instabilities are now more apparent.

Both of the previous features—constant-voltage turn-off and pulse instabilities—result from the highly discrete nature of the individual quantum states in our structure. In actuality, we have composed a QC structure out of only six relevant states: a ground state for each of the five

quantum wells in the QC period and one quantum well first-excited state that is the upper laser state. Having only six states spread across $\Delta = 107$ meV is unusual for QC structures; a comparable injector wells would have 12 states spread across the same Δ . In this situation, we see the effect of the highly discrete injector region states; the positioning of individual states matters more than ever.

2.4.3.3. Device Performance

Even with all of the unique features of the present device, performance is comparable to the best designs reported in the literature. We observe lasing at $\lambda \sim 5.0$ μm for $T_{\text{sink}} = 79$ K and at $\lambda \sim 5.2$ μm at room temperature, as shown in Fig. 22a. For the BH laser device described by the Figs. 21 and 22 data, pulsed total output power peaks at 3.9 W at 180 K, while room temperature output power is 1.4 W. Low temperature output power in these devices is severely limited by the pulse instabilities previously discussed. Threshold current density is as low as 460 A/cm² at 80 K, and grows to 2.3 kA/cm² at room temperature. Figure 22b shows threshold behavior similar to the three injector well design. As in the three injector well device, the T_0 approaching room temperature is relatively low at 113 K; the low temperature $T_0 = 305$ K. Wallplug efficiency—as shown in Fig. 22c—peaks at 23.0% for $T_{\text{sink}} = 140$ K and 7.6% at 300 K. Again, wall-plug efficiency at low temperatures is limited by pulse instabilities.

2.4.4. Conclusions

In this sub-project, we studied short injector region QC lasers, taking the approach of shrinking the conventional (approximately) seven quantum well injector region to only two or three wells. Making the active core gain region “denser” with optical transitions by shortening the QC period length in principle leads to improvement in performance metrics associated with output power and efficiency. Through this study of short injectors, we have observed several unique effects in QC lasers. While the understanding of these effects augments our knowledge of QC laser processes in general, they are particularly relevant with regard to developing high performing lasers based on the short injector concept.

Pronounced NDR is observed in spontaneous emission EL devices; furthermore, the presence of stimulated emission in laser devices of the same QC design impacts the operating configuration of the laser band structure. Turn-off mechanisms—increases in differential resistance—are observed at constant voltages with temperature, in addition to the more conventional turn-off features observed at constant current. These effects can be attributed to two distinctive characteristics of the short injector designs presented here: enhanced “coupling” of neighboring active regions due to the close proximity afforded by the extremely abbreviated injector regions; and the highly discreet nature of the injector region energy states.

The observation of these new phenomena provides additional insight into the mechanisms of QC laser operation. The pronounced NDR of the three injector well laser and its successful operation at a lowered field demonstrates the dynamic effect of stimulated emission on electron distributions and energy state lifetimes. Indeed, much of what we have observed confirms that such abbreviated QC structures behave in many ways similar to the classical semiconductor superlattice.

For example, the highly discrete nature of individual states becomes particularly relevant, as well as the need to damp pulse instabilities [42] associated with shifting charge distributions. Clearly challenges remain with optimizing QC laser injector regions. In addition to the need to damp pulse instabilities, we have observed relatively low T_0 values in short injector structures (see also [43]) that are beginning to appear to be systematic. Understanding the origin of this diminished performance at elevated temperatures will help to realize the full potential of short injector QC structures.

2.5. Modeling of interface roughness in Quantum Cascade lasers and its impact on laser performance

2.5.1. Inhomogeneous origin of the interface roughness broadening of intersubband transitions

Quantum Cascade lasers rely critically on intersubband transitions (IST's) [44,45] in semiconductor quantum wells (QWs). Their benefits result from the fact that the IST's are quite strong and can be engineered for any particular wavelength. Two factors are responsible for the strength of IST – the large optical dipole moment and a linewidth that is comparatively narrow due to nearly parabolic dispersion of the subbands. The performance of intersubband devices – and hence QC lasers – critically depends on the transition linewidth, which is determined by a combination of a number of broadening mechanisms. Often, depending on the wavelength region, temperature, and doping level, one of these broadening mechanisms dominates.

In the mid infrared range, the broadening is interface roughness broadening (IRB), as shown in [46-48]. In the 10-12 micron range linewidths well in excess of 5meV are typically measured, and this number is significantly larger than lifetime broadening due to LO phonon scattering (which is typically on the order of 1-2 meV). The IRB becomes progressively larger with the increase in the IST energy. This becomes especially important in QC lasers [45] where the states are spread out through more than one QW and thus incorporate many interfaces whose roughness is largely uncorrelated. For QC lasers operating in the 3-5 μm range a linewidth in excess of 20meV is not unusual. However, when it comes to treating the IRB one encounters a logical controversy.

Typically the IRB is treated, following Ando [49, 50], as lifetime broadening due to elastic scattering of conduction electrons [48] – the broadening is then purely homogeneous and temperature independent. Indeed, the mostly homogeneous character of IRB has been corroborated by the lack of the experimental evidence of spectral hole burning, even at high intensities. Yet the QC laser threshold current always shows the same exponential dependence on temperature that characterizes a common interband semiconductor laser in which the transitions have different energies. This dependence can be partially explained by the band nonparabolicity [51] and thermal backfilling of the lower laser state and thermionic emission from the upper laser state, but even the lasers in which all the precautions have been taken to reduce the latter two deleterious effects still exhibit the same, exponential, thermal dependence.

While the momentum scattering model of Ando is most conducive to evaluation of transport properties, in the determination of optical properties this would not necessary be the best method. The potential energy, while randomized in space, is still independent of time – hence a set of stationary eigenstates should be sufficient to fully characterize the system. Vasko [52] had used

this approach and had obtained the inhomogeneously broadened line shapes with linewidths that are within an order of magnitude of the experimental ones. Yet the results of [52] also predict that a spectral hole can be burnt in the IST and this clearly contradicts most of the available experimental data.

More recently [53, 54] a different model was proposed in which the IST's were treated as second order processes involving an intermediate virtual state. In this model both energy and momentum are conserved and the asymmetric shape of gain has been predicted and experimentally verified [55, 56]. Nevertheless, while using a time dependent perturbation theory is a sound technique when dealing with a time dependent perturbations, like phonons, its use is questionable when it comes to the time independent perturbation such as interface roughness. One should expect that introduction of roughness should simply create new set of time-independent eigenfunctions and the broadening shall appear as a result of transitions between these new eigenfunctions. To the best of our knowledge no such explanation for the IRB exists.

In this sub-project we develop a simple model for calculating IRB using variational principle. The IRB causes the eigenstates to be spread out in the momentum space which in turn leads to possibility of the non-vertical IST's and thus to effective inhomogeneous broadening of IST energy. We also show that despite the fact that the IRB is caused by the spatial inhomogeneity of the interface, the hole burning cannot occur. We give a simple explanation for co-existence of gain and absorption in the QCL observed in [55, 56] and also predict interesting phenomena of motional narrowing in the regime of strong IST-light coupling.

First of all we introduce surface roughness potential for the n -th subband described by the envelope function $\varphi_n(z)$ as $V_n(\mathbf{r}) = \sum_i \delta U(z_i) \varphi_n^2(z_i) h_i(\mathbf{r})$ where $\delta U(z_i)$ is the band offset at i -th interface, and the interface roughness height is described by a correlation function

$\int h(\mathbf{r} - \mathbf{r}_1) h(\mathbf{r}) d\mathbf{r} = \Delta^2 e^{-r^2/\Lambda^2}$ with mean square roughness Δ and correlation length Λ . Fourier

transform of the correlation function yields the 2D power spectrum of the perturbation

Hamiltonian, $\langle |V_{q,n}|^2 \rangle = V_{0,n}^2 \Lambda^2 e^{-\frac{\Lambda^2 q^2}{4}}$ where $V_{0,n}^2 = \Delta^2 \left(\sum_i \delta U^2(z_i) \varphi_n^2(z_i) \right)^2$ assuming that the roughness at different interfaces is uncorrelated [48].

The perturbation potential V mixes the states with different k -vectors. Clearly, all the degenerate states with the same energy E_{k0} can be mixed with no penalty and then there will be also mixing of states \mathbf{k} ($k \neq k_0$) with different energies as shown in Fig.23(a). The new wave function with the “central” wave vector k_0 can then be written as $f_{k_0n}(\mathbf{r}) = \int F(k_0, \mathbf{k}) e^{i\mathbf{k} \cdot \mathbf{r}} d\mathbf{k}$. Since the perturbation is random it can only be described by the autocorrelation (coherence) length L_c . The electron density spectrum of the mixed state is then

$$\langle |F(k_0, \mathbf{k})|^2 \rangle = \frac{1}{(2\pi)^{3/2} k \delta k} e^{-\frac{(k_0 - k)^2}{2\delta k^2}} \quad (4)$$

where $\delta k = L_c^{-1}$ shown in Fig.23(a). And shown in Fig.23(b) is an example of an instant electron density distribution for a typical random state. Next we estimate the mean square of the change of the potential energy caused by the mixing

$$\begin{aligned} \langle \delta U_{p,n}^2(k_0) \rangle &= \left\langle \left| \int f_{kn}(\mathbf{r}) V(\mathbf{r}) f_{kn}^*(\mathbf{r}) d\mathbf{r} \right|^2 \right\rangle = \\ &= \left\langle \int \int \int |V_{k_1-k_2,n}|^2 F(k_0, \mathbf{k}_1) F^*(k_0, \mathbf{k}_2) F^*(k_0, \mathbf{k}_3) F(k_0, \mathbf{k}_3 + \mathbf{k}_2 - \mathbf{k}_1) d\mathbf{k}_1 d\mathbf{k}_2 d\mathbf{k}_3 \right\rangle \end{aligned} \quad (5)$$

where we have used the fact that $\langle V(\mathbf{q}_1) V^*(\mathbf{q}_2) \rangle = |V_q|^2 \delta(\mathbf{q}_1 - \mathbf{q}_2)$. At this point we assume that the roughness has a relatively small scale, i.e. $2\Lambda k_{\max} \ll 1$ where k_{\max} is the maximum electron wave vector of the order of $k_{\max} \sim \hbar^{-1} \sqrt{2m_c k_B T} \sim 0.3 \text{ nm}^{-1}$ - i.e. $\Lambda \sim 1 \text{ nm}$ is assumed to be somewhat less than 1nm. Then $\langle |V_{q,n}|^2 \rangle = V_{0,n}^2$ and

$$\langle \delta U_{p,n}^2(k_0) \rangle = V_{0,n}^2 \Lambda^2 (2\pi)^{3/2} k_0 \delta k \quad (6)$$

The expected variation in kinetic energy can be found as

$$\langle \delta U_{kin,n}^2(k_0) \rangle = \left\langle \left(\frac{\hbar^2 k^2}{2m_c} \right)^2 \right\rangle - \left(\frac{\hbar^2 k_0^2}{2m_c} \right)^2 = 6 \left(\frac{\hbar^2}{2m_c} \right)^2 k_0^2 \delta k^2 \quad (7)$$

Since the total number of states that get mixed by the roughness potential is $N_{mix} \sim k_0 \delta k$ the meaning of (6) and (7) is rather clear – on one hand the potential energy changes as $N_{mix}^{1/2}$ while kinetic energy changes as N_{mix} itself. According to the variational principle actual eigenstate will occur when the total energy goes through extreme, i.e. it when the changes in potential and kinetic energies balance each other. Differentiating (6) and (7) over δk we readily obtain

$$\delta k = \left(\frac{m_c V_{0,n} \Lambda}{\hbar^2} \right)^2 \frac{(2\pi)^{3/2}}{3} k_0^{-1} = L_c^{-1} \quad (8)$$

If we now equate L_c with the mean free path for the electron we can obtain the mean scattering time as

$$\tau_{s,n} = \frac{m_c L_c}{\hbar k_0} = \frac{3}{(2\pi)^{3/2}} \frac{\hbar^3}{m_c} V_{0,n}^{-2} \Lambda^{-2} \quad (9)$$

Using (9) and Kubo-Greenwood formalism [57, 58] we can obtain the expression for the conductivity [57, 58] that is no different from the classical result in [49], but here we are interested only in the broadening of the level n (Fig.23a)

$$\Gamma_n = \hbar \tau_{s,n}^{-1} = \frac{2\sqrt{2\pi}}{3} \frac{\pi m_c}{\hbar^2} V_{0,n}^2 \Lambda^2 \quad (10)$$

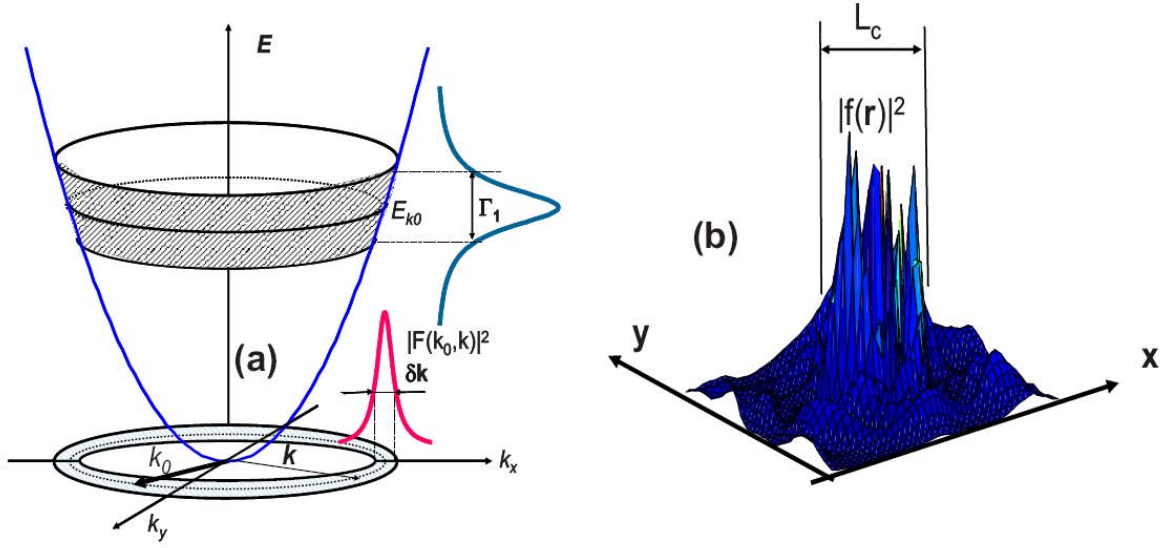


Fig.23: a. Electron density spectrum of the states mixed due to interface roughness. **b.** Snapshot of a typical random mixed wave function.

which almost exactly equals the one estimated in [48] with a small (factor of 1.6) difference that can be ascribed to using Gaussian rather than Lorentzian shape.

Let us now consider the sum of matrix elements of the IST between the state- $|1, k_{01}\rangle$ in the lower subband all the states $|2, k_{02}\rangle$ in the interval dk_{02} around k_{02} in the upper subband (Fig.24a), first assuming that there is no correlation between broadenings of these two states.

$$d\langle P_{k_{10}k_{20}}^2 \rangle = d\langle | \langle 1, k_{01} | P | 2, k_{02} \rangle |^2 \rangle = P_0^2 \sum_k \langle |F(k_{01}, \mathbf{k})|^2 \rangle \langle |F(k_{02}, \mathbf{k})|^2 \rangle = \frac{P_0^2 e^{\frac{(k_{01}-k_{02})^2}{2\delta k_{12}^2}} dk_{02}}{(2\pi)^{1/2} \delta k_{12}} \quad (11)$$

where P_0 is the IST momentum matrix element between original states $|1, k\rangle$ and $|2, k\rangle$ and $\delta k_{12}^2 = \delta k_1^2 + \delta k_2^2$. As one can see the momentum conservation is violated by the interface localization with the total momentum uncertainty equal to the sum of uncertainties of each band. But the interface roughness affects two subbands in a similar fashion therefore the states $|1, k_{01}\rangle$ and $|2, k_{02}\rangle$ are actually correlated and as a result broadening δk_{12} in (11) is less than a sum of two individual broadenings. In fact, if the interface broadening had affected two bands equally then the two wavefunctions $f_{k_{01}1}$ and $f_{k_{02}2}$, would have been identical, and, since all the states in a given subband are orthogonal, there would have been a delta function $\delta(k_{01} - k_{02})$ in (11). Of course, the correlation is not complete, as the upper subband state, with larger barrier penetration, is more affected by the interface roughness than the lower one, hence one shall use the difference between the scattering potentials of two subbands [48]

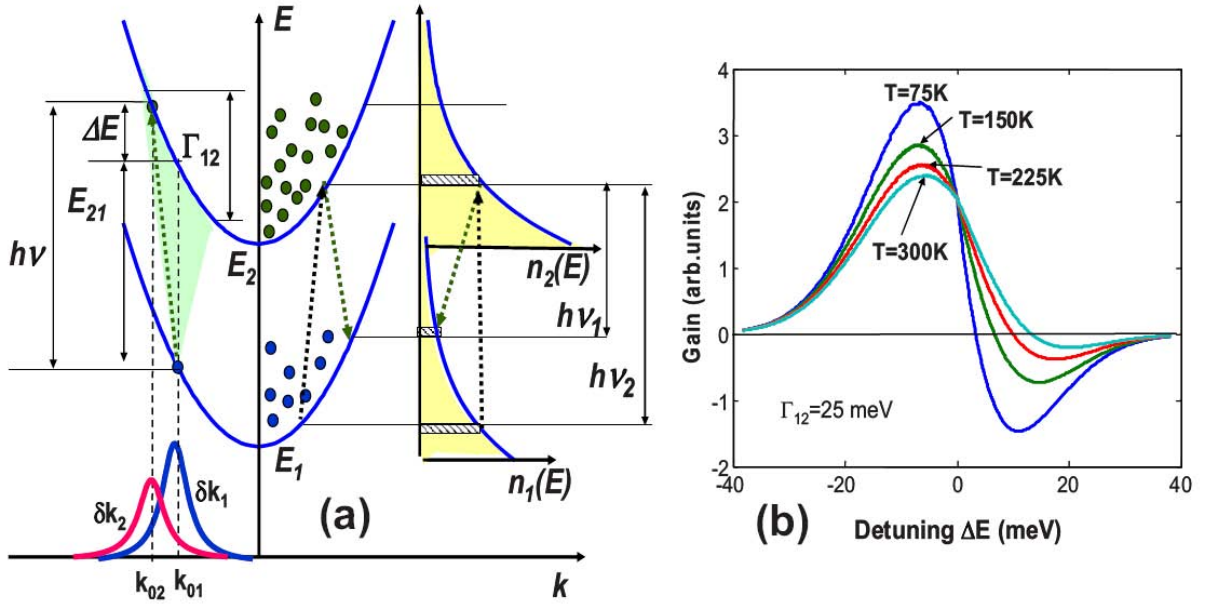


Fig.24: **a** Left hand side: allowed transitions between the states mixed by interface roughness. Right hand side: Absorption and emission between two subbands and their populations as function of energy. **b.** Gain and absorption spectra of the IST in QC lasers for different temperatures.

$V_{0,12} = \Delta^2 \delta U^2(z_i) \left(\sum_i [\varphi_1^2(z_i) - \varphi_2^2(z_i)] \delta U^2(z_i) \right)^2$ in estimating δk_{12} which according to (8) yields

$$\delta k_{12} = \left(\frac{m_c V_{0,12} \Lambda}{\hbar^2} \right)^2 \frac{(2\pi)^{3/2}}{3} k_{01}^{-1} \quad (12)$$

Now one can calculate the rate of IST from a state $|1, k_{01}\rangle$ to the upper subband caused by photons with energy $\hbar\omega$ separated from the resonant IST energy E_{12} by detuning ΔE as

$$\tau_{12}^{-1}(\omega) = \frac{2\pi e^2 A^2}{\hbar m_0^2} \int \delta \left(\hbar\omega - E_{12} + \frac{\hbar^2(k_{01}^2 - k_{02}^2)}{2m} \right) d \langle P_{k_{01}k_{02}}^2 \rangle = \frac{2\pi e^2 A^2}{\hbar m_0^2} \frac{P_0^2}{\sqrt{2\pi} \Gamma_{12}} e^{-\frac{(\Delta E)^2}{\Gamma_{12}^2}} \quad (13)$$

where A is the vector potential, and the IST broadening, shown in Fig.24a

$$\Gamma_{12} = \frac{2\sqrt{2\pi}}{3} \frac{\pi m_c}{\hbar^2} V_{0,12}^2 \Lambda^2 \quad (14)$$

is close to the one in [48]. It is also clear that although the broadening is inhomogeneous in nature, every occupied state is equally excited by radiation with a given detuning from resonance, thus no spectral hole burning can be observed – therein lies the difference between IRB where the momentum selection rules are relaxed and the broadening due to non-parabolicity [51] where they are preserved. Now, if one considers the QC laser case, in which both subbands

are populated (right hand side of Fig.24a) one can see the Stokes shift between absorption and gain since at positive detuning ΔE the kinetic energy of the state in the upper subband is higher than that of the electron in the lower subband, hence the upper state population decreases and the probability of absorption increases. This co-existence of gain and absorption is also shown in Fig.24b for different temperatures for the case when 2/3 of the carriers occupy upper subband. It confirms the results obtained in [53-56], despite the fact that we have treated the IRB as an inhomogeneous process. It also can be seen from Fig.24b that the apparent gain linewidth increases with temperature despite the fact that actual IST linewidth does not change at all.

At this point it is reasonable to ask a question: other than offering an alternative (and in our opinion more physical) insight into the nature of IRB of IST, but otherwise yielding the same observable results, does our inhomogeneous model predict any new phenomena that cannot be explained with a standard scattering model? The answer can be found when one consider the case of strong coupling between the IST and light – that of the IST polariton which had recently attracted significant attention [59-62] following the initial observations in [63]. When the coupling between the light and IST (measured by Rabi splitting) becomes comparable and then larger than broadening Γ_{12} the intersubband excitations with different resonant energies get coupled together with a photon into a new state - polariton whose broadening is actually less than Γ_{12} .

In conclusion, we have described an alternative approach to the IRB of the IST in semiconductor QW's by treating it as a localization problem. Our results not only offer clear physical explanation for the coexistence of gain and absorption in QC lasers that agrees with prior work, but also predict new effects in the regime of strong IST – photon coupling.

2.5.2. Role of interface roughness in the transport and lasing characteristics of Quantum Cascade lasers.

Fundamentally, one period of a QCL (Fig.25) incorporates an active region with an upper (*u.l.*) and lower (*l.l.*) lasing levels, and one or more “dumping” levels separated from the lower laser level by a few phonon energies [64] to assure quick depopulation of *l.l.* Alternatively, there *l.l.* and the dumping layers can be very closely spaced and then one ends up with a confined-to-continuum scheme [65]. Also incorporated in each period is the injector serving to quickly move the electrons into the *u.l.* of the next period. The transport through the injector is of mixed resonant and phonon-assisted tunneling nature, but the last, vital step of the transition from the lowest injector level (*i*) to the *u.l.* occurs via resonant tunneling.

The choice of the coupling between injector and *u.l.* is so critical because on one hand large coupling energy $\hbar\Omega_c$ is required to maintain high current and quickly populate *u.l.*, but, on the other hand, when the coupling becomes too large, one essentially ends up with two coupled states spanning across both injector and active regions that are split by $2\hbar\Omega_c$, which gravely affects the laser gain shape and magnitude. According to the widely accepted theory of Kasarinov and Suris [66] the resonant current density can be written as

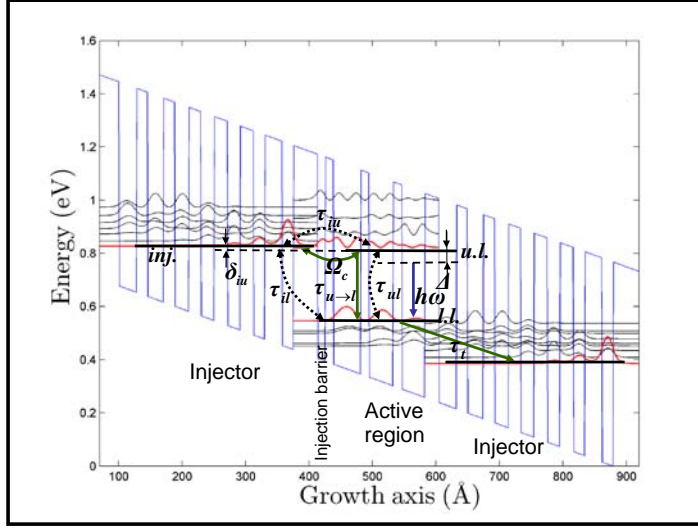


Fig.25: Energy diagram of a 4.7 μm QCL with relevant transition times indicated by the solid arrows and dephasing times indicate by the dashed arrows.

$$J = eN_s \frac{2\Omega_c^2 \tau_{\perp}}{1 + \delta_{iu}^2 \tau_{\perp}^2 + 4\Omega_c^2 \tau_{u \rightarrow l} \tau_{\perp}} \quad (15)$$

where N_s is doping density per period, δ_{iu} is the detuning of tunneling transition, $\tau_{u \rightarrow l}$ is the $u.l.$ lifetime and τ_{\perp} is the momentum relaxation time in the QW plane, usually related to the in plane mobility. This time is also responsible for the broadening of the laser gain [67] and luminescence. Based on (15) it is desirable to have coupling strong enough that the maximum current is determined only by τ_{ul} , i.e. $\Omega_c \gg (\tau_{ul} \tau_{\perp})^{-1/2}$ [68], yet the coupling should not exceed the gain broadening to avoid the splitting of gain in two, hence one must maintain $\Omega_c \ll \tau_{\perp}^{-1}$. This trade-off yields optimized $\Omega_c \sim \tau_{u \rightarrow l}^{-1/4} \tau_{\perp}^{-3/4}$, which for typical values of $\hbar \tau_{\perp}^{-1} \sim 10 \text{ meV}$ and $\hbar \tau_{u \rightarrow l}^{-1} \sim 0.3 \text{ meV}$ yields desired splitting between two coupled levels $2\hbar \Omega_c \leq 10 \text{ meV}$ as is indeed done in most successful designs.

The original approach [69] did not specify the origin of in-plane momentum relaxation (broadening) which was assumed to be equal for all transitions, optical or tunneling ones. But in mid-IR QC lasers the main origin of broadening is interface roughness as discussed in the previous section, and it is well known that different transitions see different broadenings. The interface roughness broadening of the transition between two levels described by the envelope wave-functions $\varphi_m(z)$ and $\varphi_n(z)$ can be written as [70, 71]

$$\hbar \tau_{m,n}^{-1} = \frac{2\sqrt{2\pi}}{3} \frac{\pi m_c}{\hbar^2} \Delta_h^2 \Lambda^2 \left(\sum_i \delta U^2(z_i) [\varphi_n^2(z_i) - \varphi_m^2(z_i)] \right)^2 \quad (16)$$

where $\delta U(z_i)$ is the band offset at i -th interface, and the interface roughness height is characterized by mean square roughness Δ_h and correlation length Λ . Thus in the QC laser of

Fig.25 the broadening (dephasing) of the vertical lasing transition, $\hbar\tau_{ul}^{-1}$ where both levels are localized in the active region is substantially lower than the broadening of diagonal transition $\hbar\tau_{ii}^{-1}$ [71] and tunneling transition $\hbar\tau_{iu}^{-1}$, where two states are localized in different regions. The width of the lasing transition can be obtained from the luminescence measurements – then the widths of all other transition can be found by scaling using (16), and we indeed obtain quite different FWHM broadenings, $2\hbar\tau_{ul}^{-1} \sim 21\text{meV}$, $2\hbar\tau_{iu}^{-1} \sim 98\text{meV}$ and $2\hbar\tau_{il}^{-1} \sim 66\text{meV}$, which are all in turn much broader than the lifetime broadening $\hbar\tau_{u \rightarrow l}^{-1} < 1\text{meV}$. These disparities are of great consequence to the QC laser design.

To fully understand this we have solved the complete density matrix equation for the three-level system of Fig.25 in which tunneling characterized by coupling strength $\hbar\Omega_c$ and optical transitions caused by laser field of intensity I_l occur simultaneously,

$$\begin{aligned} \frac{d}{dt} \begin{pmatrix} \rho_{ii} & \rho_{iu} & \rho_{il} \\ \rho_{ui} & \rho_{uu} & \rho_{ul} \\ \rho_{li} & \rho_{lu} & \rho_{ll} \end{pmatrix} = j \left[\begin{pmatrix} \rho_{ii} & \rho_{iu} & \rho_{il} \\ \rho_{ui} & \rho_{uu} & \rho_{ul} \\ \rho_{li} & \rho_{lu} & \rho_{ll} \end{pmatrix}, \begin{pmatrix} \delta_{ii} & \Omega_c & 0 \\ \Omega_c & 0 & \Omega_l \cos \omega t \\ 0 & \Omega_l \cos \omega t & -(\omega - \Delta) \end{pmatrix} \right] - \\ - \begin{pmatrix} -\beta^{-1}\rho_{li}\tau_t^{-1} & \rho_{iu}\tau_{iu}^{-1} & \rho_{il}\tau_{il}^{-1} \\ \rho_{ui}\tau_{iu}^{-1} & \rho_{uu}\tau_{u \rightarrow l}^{-1} & \rho_{ul}\tau_{ul}^{-1} \\ \rho_{li}\tau_{il}^{-1} & \rho_{lu}\tau_{ul}^{-1} & \rho_{ll}\tau_t^{-1} - \beta\rho_{uu}\tau_{u \rightarrow l}^{-1} \end{pmatrix} \end{aligned} \quad (17)$$

where Δ is detuning of transition frequency ω_{ul} from optical field frequency ω , lasing Rabi frequency is $\hbar\Omega_l = (2\eta_0 e^2 z_{ul}^2 I_l / n)^{1/2}$, $\eta_0 = 377\Omega$, z_{ul} is the dipole matrix element, τ_t is the effective injector transport time, and $\beta(T) < 1$ is the lower laser state thermal backfilling parameter. Using the latter two parameters allows us to avoid explicit incorporating in the density matrix equation all the injector levels except the last one.

Proceeding with a standard steady state solution we can obtain the expression for the steady-state gain coefficient $\gamma = 8\pi\alpha_0 N_s z_{ul}^2 \omega / \Omega_l d n \times \text{Im}(\rho_{ul} e^{-j\omega t})$, where d is the thickness of one period of QCL, n is refractive index, and α_0 is a fine structure constant. For the case of laser being at or near threshold, $\Omega_l \sim 0$ we obtain

$$\gamma = \gamma_0 \frac{2\Omega_c^2 \tau_{iu} \tau_p}{1 + \delta_{iu}^2 \tau_{iu}^2 + 2\Omega_c^2 \tau_{iu} \tau_p} \times \frac{\left[1 + \Delta^2 \tau_{il}^2 + \Omega_c^2 \tau_{il} \tau_{ul} \right] + \frac{\tau_{il} (1 + \delta_{iu}^2 \tau_{iu}^2)}{\tau_{u \rightarrow l} - \beta \tau_t} \left[1 + (\Omega_c^2 - \Delta^2) \tau_{il} \tau_{ul} \right]}{\left[1 + (\Omega_c^2 - \Delta^2) \tau_{il} \tau_{ul} \right]^2 + \Delta^2 [\tau_{il} + \tau_{ul}]^2} \quad (18)$$

where $\tau_p = 2\tau_{u \rightarrow l} + \tau_t$ is the minimum pass time through one period,

$\gamma_0 = 4\pi\alpha_0 z_{ul}^2 \omega \tau_{ul} N_s (\tau_{u \rightarrow l} - \beta \tau_t) / \tau_p d n$ is the maximum gain. The first term in (18) characterizes the resonant tunneling current dependence on voltage (via δ_{iu}). In contrast to (15) it contains a very short dephasing time τ_{iu} associated with localization in different regions, rather than much longer laser transition dephasing time τ_{ul} that is measured in luminescence experiments.

Furthermore, gain saturation depends not just on *u.l.* lifetime $\tau_{u \rightarrow l}$ but also on the transport time τ_t of injector. Hence maximizing of current calls for $\Omega_c \gg (\tau_{iu} \tau_p)^{-1/2}$. The width of resonant tunneling peak (nearly 100 meV) indicates that rather than exhibiting negative differential resistance (NDR) the current in QC lasers should simply saturate as is indeed the case in most experiments. One can easily interpret the absence of NDR region as the result of localization [72].

The second term in (18) characterizes the line shape and it has two components. The first component represents the splitting of the upper laser level due to coupling with injector which becomes observable only when $\Omega_c \sim (\tau_{ul} \tau_{il})^{-1/2}$, i.e. with considerably stronger coupling than what one would expect based on the linewidth of lasing transition τ_{ul}^{-1} obtained from the luminescence or absorption measurements. The second component of the numerator in (18) represents stimulated coherent transfer of population directly from the injector to the lower laser level – one can think of this process as a stimulated Raman process in which the role of the pump is played by tunneling current. Since the upper level lifetime $\tau_{i \rightarrow u}$ is at least an order of magnitude longer than the dephasing time τ_{il} , the coherent term plays very small role and presents mostly an academic interest for the MWIR QC.

The plot of gain vs. coupling strength (18) for $\Delta=0$ and $\tau_t \sim 2ps$ (estimated as the time for emission of successive six optical phonons [67]) is shown in Fig.26 and exhibits a steep rise followed by a rather gentle fall off and simple optimization show that the maximum is reached when $2\hbar\Omega_c \sim \hbar(\tau_p \tau_{iu} \tau_{il} \tau_{ul})^{-1/4}$, i.e. it is essentially a geometric mean of all the broadenings in the system. For a typical mid-IR QCL of Fig.25 with parameters mentioned above, it yields optimal splitting of 18 meV. When the QCL with newly optimized splitting had been fabricated it has indeed shown excellent maximum current and low temperature wall-plug efficiency of up to 34% [73].

It is worthwhile to point out that the large (factor of 3) disparity of dephasing times τ_{ul} and τ_{il} leads to an interesting phenomenon of the line shape of gain (and luminescence) broadening rather splitting into two due to coupling between injector and upper level. This is simply the result of upper laser level wave function spreading into the injector region where it is affected by the roughness that is completely uncorrelated with roughness of the lower laser level – hence less of “subtraction” in expression (2) takes place and the apparent linewidth widens to more or less geometric mean $(\tau_{ul} \tau_{il})^{-1/2}$. One may compare this phenomenon with the tunneling induced transparency – equivalent of electromagnetically induced transparency (EIT) first observed in intersubband transitions in [74] when the effective linewidth of a relatively broad transition had been narrowed due to admixing of a very narrow transition. Thus here we are dealing with the exact opposite of EIT. As the tunneling resonance is detuned the linewidth returns to the original narrow linewidth τ_{ul}^{-1} of decoupled transition as shown in Fig.27 and has been indeed observed in [70].

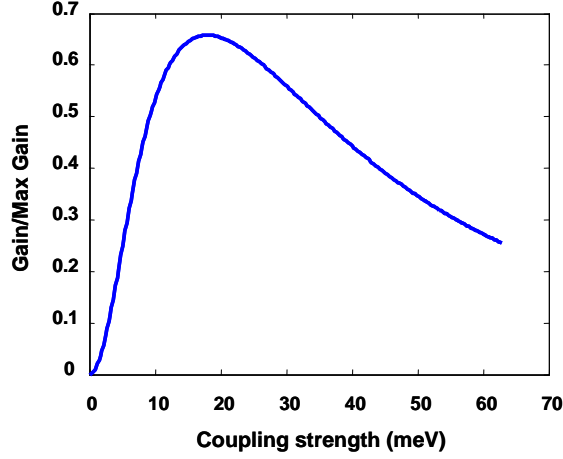


Fig.26: The gain coefficient as a function of energy level splitting $2\hbar\Omega_c$ in QCL of Fig.25

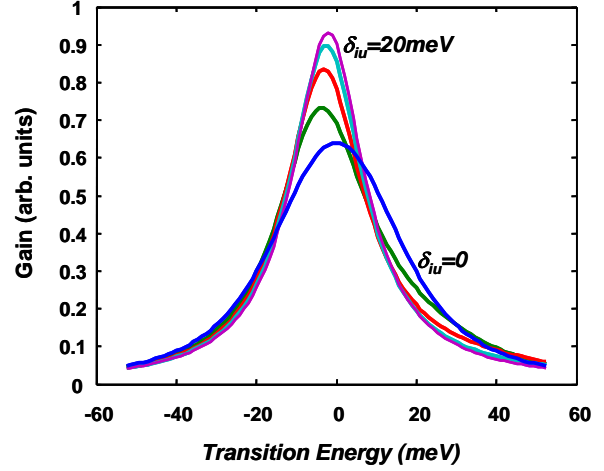


Fig.27: The shape of laser linewidth for different detuning between injector and upper laser level.

In conclusion, we have developed a rigorous density-matrix model for current and gain in QCL that takes into account the disparity between different dephasing times cause by interface roughness. Using the theory we have shown that the coupling between injector and upper laser level should be much stronger than previously accepted values. These conclusions had been verified experimentally.

2.5.3. Effective transit time in high performance Quantum Cascade lasers including the photon density

In this section, we present an extended model of WPE by including the resonant injection of carriers into the upper laser level in a density-matrix framework.

The conduction band diagram of a conventional QC laser structure considered here is shown in Fig. 25 above, where the injector ground, upper laser, and lower laser levels are highlighted. We have presented a density-matrix model involving those three levels and calculated the steady-state gain near threshold in the previous section [75]. The results showed how the injection coupling strength affects the peak gain and the width of the gain profile. The primary conclusion was that the large broadening of the tunneling transition requires a stronger injection coupling than previously used in conventional designs.

Here, we complete the laser model by taking into account the photon number density in the cavity that balances gain and loss. For simplicity, we treat the laser transition through scattering processes in the density matrix equations but retain the coherence and dephasing of the tunneling transition. The maximum current density J_{\max} at injection resonance is expressed in terms of an effective transit time τ_{trans} as $J_{\max} = eN_s/\tau_{\text{trans}}$, where N_s is the sheet doping density. The result for the effective transit time is given by

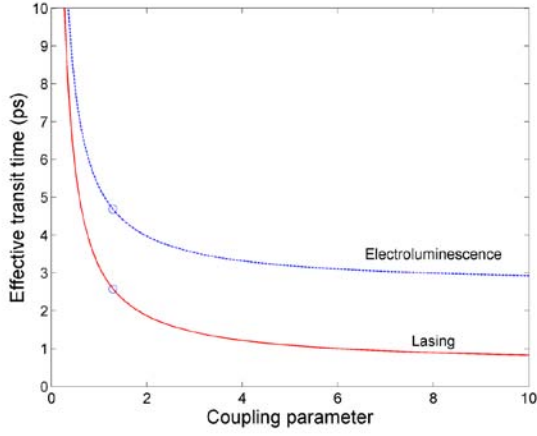


Fig. 28: Effective transit time as a function of the dimensionless coupling parameter ($4\Omega_c\tau_\perp\tau_u$) for the structure shown in Fig. 25.

$$\tau_{\text{trans}} = \eta_{\text{tr}}\tau_u \frac{1 + \frac{\tau_{li}}{\tau_{\text{up}}}(1 + 6\Omega_c^2\tau_\perp\tau_u)}{2\Omega_c^2\tau_\perp\tau_u} \quad (19)$$

where η_{tr} is the differential efficiency of the laser transition, τ_u is the total scattering time out of the upper laser level, τ_{li} is the effective transit time from the lower laser level to the injector ground state, τ_{up} is the effective upper level lifetime, Ω_c is the frequency corresponding to the injection coupling energy $\hbar\Omega_c$, and τ_\perp is the dephasing time of the tunneling transition. Figure 28 shows the effective transit time for the QCL structure of Fig. 25 as a function of the dimensionless coupling parameter ($4\Omega_c\tau_\perp\tau_u$), as well as the transit time for an electroluminescent device based on the same structure. The difference between the two curves corresponds to the improvement in transit time and maximum current enabled by the presence of cavity photons in a laser. The circles identify the transit times for the particular coupling energy employed by this structure, and the results show that the current efficiency and therefore the wallplug efficiency of the laser can be improved by employing stronger injection coupling.

2.6. Intersubband absorption loss in high performance Quantum Cascade lasers

Waveguide loss is a critical parameter for performance and WPE improvements in QC lasers, since any excess waveguide loss increases threshold current densities and limits the efficient extraction of generated light out of the laser cavity [76]. Recent temperature-dependent measurements of waveguide loss have pointed to the dominant contribution of resonant intersubband absorption in the active core [77]. Here, we analyze two high-performance QCL designs in terms of intersubband absorption loss, and report measured waveguide loss for lasers based on these two designs.

We start with a numerical solution of Schroedinger's equation for multiple stages of a QC laser structure to find both the bound and the quasi-bound state wavefunctions. The absorption loss due to multiple intersubband transitions is calculated from a double summation over initial and final states using

$$\alpha_{\text{ISB}}(\omega) = \frac{4\pi e^2}{\epsilon_0 n_{\text{eff}}} \frac{\pi}{2L_p} \sum_i N_i \sum_j \frac{\langle z_{ji} \rangle^2}{\lambda_{ji}} \frac{\gamma_{ji}/\pi}{(E_{ji} - \hbar\omega)^2 + \gamma_{ji}^2} \quad (20)$$

where L_p is the length of one period of the structure and λ_{ji} , $\langle z_{ji} \rangle$, E_{ji} , and γ_{ji} are the wavelength, dipole matrix element, transition energy, and linewidth, respectively, of each intersubband transition included in the summation. The carrier densities N_i are assumed to follow a thermal distribution among the initial states, starting with the injector ground state. The linewidth for each transition is found by using a model of interface-roughness broadening [78, 79] and is given by

$$\gamma_{ji} = \frac{\pi m^*}{\hbar^2} \Delta^2 \Lambda^2 \delta U^2 \sum_m \{ \psi_i^2(z_m) - \psi_j^2(z_m) \}^2 \quad (21)$$

where Δ is the average roughness height, Λ is the roughness correlation length, δU is the conduction band offset, and $\psi_i(z_m)$ are the wavefunction values at the interfaces. For this study, an interface parameter product of $\Delta\Lambda = 1.04 \text{ nm}^2$ was used, which is comparable to values reported earlier [78].

Figure 29(a) shows the conduction band diagram for a QC laser structure designed to have low voltage defect for improved voltage efficiency. The transition highlighted in green that originates from the upper laser level makes the primary contribution to loss, and any intersubband absorption that would be resonant with the laser transition is avoided. The second QC laser structure was designed to have strong coupling between the injector ground state and the upper laser level, and its conduction band diagram is shown in Fig. 29(b). An additional contribution to loss in this design comes from the transition highlighted in red that involves the injector ground state.

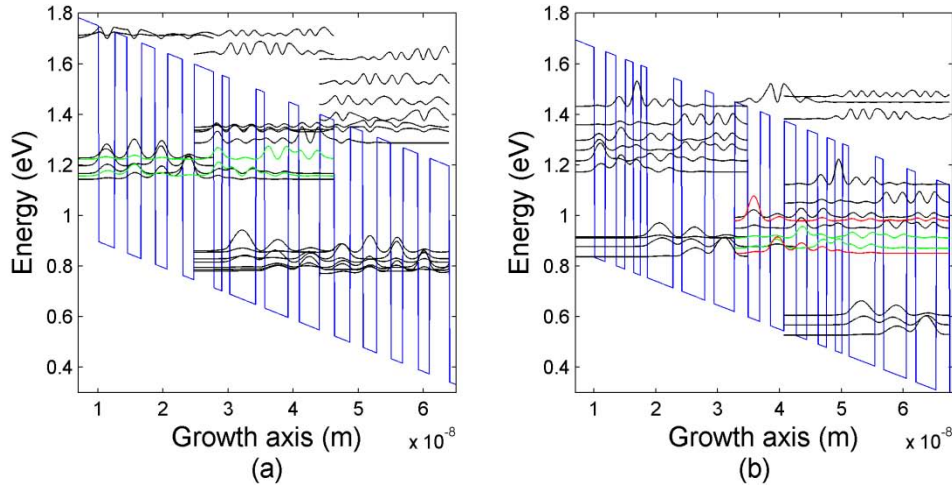


Fig. 29: (a) Conduction band diagram for the low voltage defect QC laser design; (b) conduction band diagram for the QC laser design with strong coupling. Highlighted transitions make significant contributions to intersubband absorption loss.

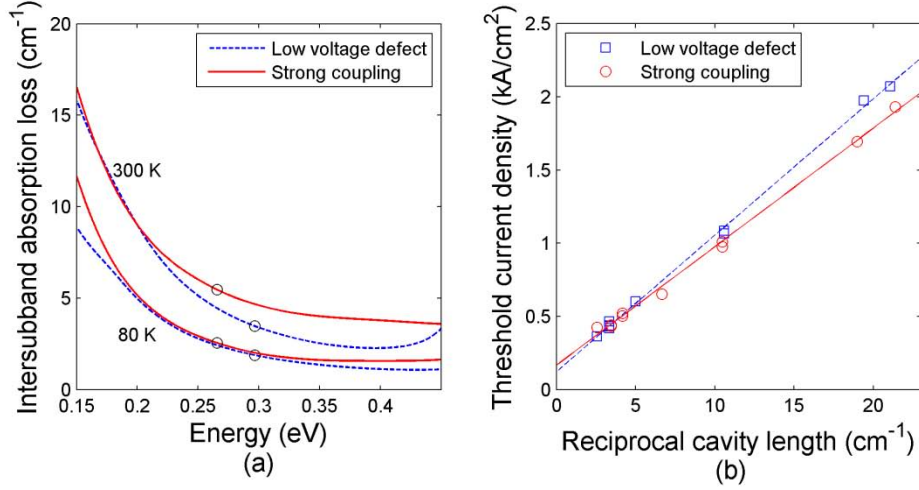


Fig. 30: (a) Calculated intersubband absorption loss for the low voltage defect and strong coupling designs as functions of the transition energy at two different temperatures. (b) Measured threshold current density versus reciprocal cavity length at 80 K for the two designs.

The intersubband absorption loss for the two designs calculated at two different temperatures for an injector sheet doping density of $1 \times 10^{11} \text{ cm}^{-2}$ are shown in Fig. 30(a). The loss at 80 K is found to be 1.9 cm^{-1} for the low voltage defect design and 2.5 cm^{-1} for the strong coupling design at the corresponding laser transition energies. The higher emission energy of the low voltage defect design helps to reduce the intersubband absorption loss. Cavity length dependence of measured threshold current density shown in Fig. 30(b) for lasers that were grown and fabricated based on the two designs yielded the following waveguide loss values at 80 K: 1.7 cm^{-1} for the low voltage defect design and 2.5 cm^{-1} for the strong coupling design. The measurements and the modeling results indicate that intersubband absorption loss accounts for a major component of the waveguide loss for these two designs, while the contribution from free-carrier absorption in the low-doped cladding is estimated to be 0.1 cm^{-1} .

2.7. Lasing induced reduction of core heating in high wall plug efficiency Quantum Cascade lasers

As already outlined repeatedly above, recent improvements in QC lasers have resulted in devices that operate with large WPE at both cryogenic and room temperatures [80]. This progress has come from better models [81], designs [80,82], and improved thermal management [80, 83]. A result of this efficient emission of light is that a substantial fraction of the input electrical power no longer contributes to the heating of the active core. This reduction in heating is highly desirable since elevated core temperatures can dramatically limit QC laser performance, to the point of thermal roll-over [81]. Understanding and harnessing this lasing-induced reduction in heating may enable further improvements in laser performance.

Studies of the thermal behavior of QC lasers using noninvasive methods, such as interferometry or microprobe luminescence, have previously been reported. [84-86]. Here, we were interested

in only the lattice temperature of the QC laser active core because the temperature effects due to large WPE are most observable in this region of the laser. We were also interested in finding a measurement technique to measure the instantaneous QC laser core temperature with less complex and specialized instrumentation. We use the temperature-dependent threshold as an indicator of the active core temperature. For a laser operated in CW mode, this is accomplished by superimposing low duty cycle pulses on a core-heating DC baseline [87], measuring the instantaneous threshold current, and relating the result to known threshold versus active core temperature data. Using this measurement technique, we are able to determine the instantaneous core temperature, current efficiency, and laser self-cooling from photon emission.

The lasers used in this study were grown by metal organic chemical vapor deposition (MOCVD) using strained $\text{In}_{0.669}\text{Ga}_{0.331}\text{As}$ / $\text{Al}_{0.638}\text{In}_{0.362}\text{As}$ quantum wells and barriers on an InP substrate with the net strain balanced in each period. The active core is a traditional two-phonon resonance design with an engineered optical transition energy of 270 meV similar to Ref [80]. The devices were processed as BH lasers using lateral InP regrowth and mounted epitaxial layer up to a copper holder using indium.

The laser holder was mounted to a copper heat sink in a temperature controlled, continuous flow liquid nitrogen cryostat. Ge lenses were used to collect and focus the light onto a room temperature HgCdTe detector for pulsed measurements and a thermopile for CW measurements. The pulsed measurements were performed using 100 ns pulses at 5 kHz. The results in this letter are for the best performing laser ridge, 3.0 mm long x 5.2 μm wide, and are characteristic of several other tested devices. Figure 31 shows results for CW measurements at a heat sink temperature of 80 K. At this heat sink temperature, the device has a threshold current of 165 mA, 24 % peak WPE in CW mode, and 33 % peak WPE in pulsed mode.

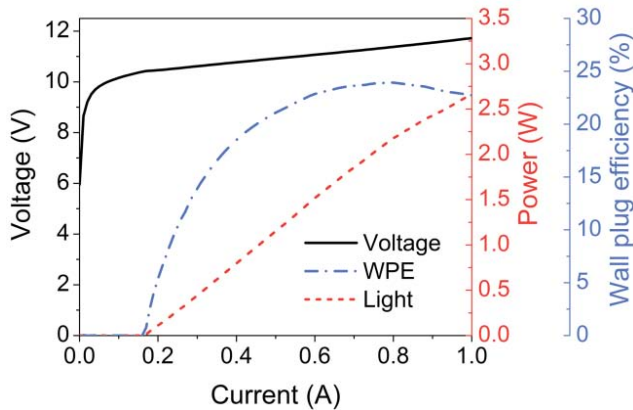


Fig. 31: Continuous wave voltage (solid, black), light (dash, red), and WPE (dot-dash, blue) versus current curves for the high efficiency device at a heat sink temperature of 80 K. The power and WPE values are reported for both facets.

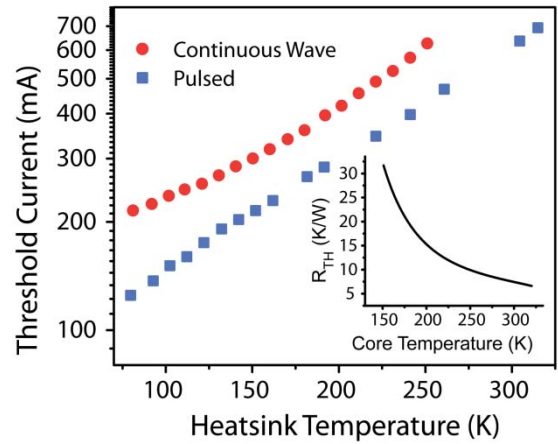


Fig. 32: Threshold current versus heat sink temperature data of the high efficiency device for CW (red circles) and pulsed (blue squares) operation. The inset shows the thermal resistance, R_{TH} , calculated from the difference in threshold currents versus temperature.

Pulsed and CW thresholds as a function of heat sink temperature are shown in Fig. 32. These thresholds were fit using high-order polynomial functions and the thermal resistance for a given

core temperature was calculated as $R_{TH}(T_{core}) = (T_{Th, pulsed} - T_{Th, CW}) / (P_{th, CW})$, where $T_{Th, pulsed}$ is the core temperature at the pulsed threshold, $T_{Th, CW}$ is the core temperature at the CW threshold, and $P_{th, CW}$ is the input power at CW threshold. The core temperature at CW threshold was determined by matching the temperature for a pulsed measurement with the same threshold current. The calculated thermal resistance is shown in the inset of Fig. 32.

To measure the instantaneous threshold current, $I_{instant}$, of the device during CW operation, the heat sink was cooled to 80 K. The temperature of the heat sink was monitored and controlled; the variation in temperature over the course of the experiment was less than 0.3 K. Light was collected onto a room temperature HgCdTe detector that was preceded by a polarizing filter to limit the amount of incident power. Pulses of 100 ns at 5 kHz were superimposed on a DC current using an impedance-matched bias-T; the very low duty cycle ensures that the pulses have a negligible effect on the temperature of the core. The center 20 ns of the current and light pulses were gated and averaged over 100 pulses. The magnitude of the low duty cycle pulses was increased every 300 ms (1500 pulses). The laser was designed to operate under negative polarity, thus for DC currents below the CW threshold, negative polarity pulses were used. Above CW threshold, positive polarity pulses were used. The polarity of the pulses was controlled by the inclusion or exclusion of an inverter immediately after the pulse generator.

Figure 33 shows measurements below and above CW threshold and the inset shows a schematic of the supplied pulses. Below CW threshold, the measurements are very similar to typical light-current measurements. However, above CW threshold, the device is turned off as larger pulses are applied. A threshold, $\delta I_{pulse, Th}$, is clearly visible for both measurements. The instantaneous threshold current of the device is given by $I_{instant, Th} = I_{DC} + \delta I_{pulse, Th}$, where I_{DC} is the DC current supplied to the device. The instantaneous current efficiency is given by $(I_{DC} - I_{instant, Th})/I_{DC}$.

To study the evolution of the instantaneous threshold at various points of CW operation (active core temperatures), the input DC power was changed and the instantaneous threshold was measured as described above. The change in the DC current was made slowly to avoid temperature fluctuations in the heat sink. The temperature of the heat sink was allowed to stabilize to fluctuations of < 0.01 K and the voltage of the QC laser, an indicator of core temperature, was allowed to stabilize to fluctuations of < 0.1 mV before recording a measurement. The maximum DC current applied was limited by the bias-T to 1 A. The minimum was limited to approximately 50 mA due to instability in the voltage for smaller DC currents. The standard deviation of the instantaneous thresholds at each CW current over the entire range of CW data is less than 1 mA. We observed a threshold dependence on the boxcar gate location of approximately 10 mA and estimate the error in our measurements to be approximately ± 5 mA.

Each of the measured instantaneous thresholds was mapped to a core temperature using the pulsed threshold versus heat sink temperature data shown in Fig. 32. Figure 34 shows the results of the measurements and mapping. Using the WPE and R_{TH} data, the core temperature was calculated. The starting core temperature of 131 K was selected to match the experimental data at the power corresponding to the onset of CW lasing, 1.8 W; no other fitting parameters were used. For the calculations, the change in core temperature, ΔT_{core} , was calculated as:

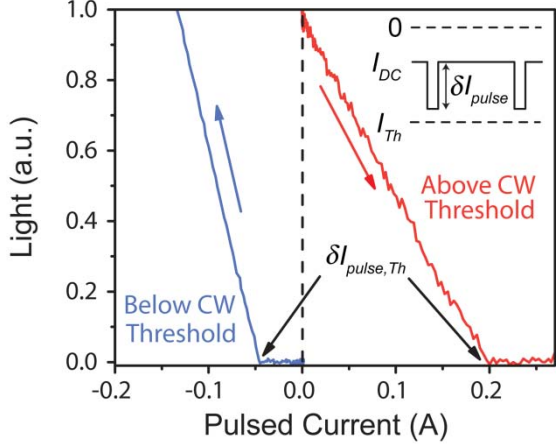


Fig. 33: Light versus pulsed current for measurements below (blue) and above (red) CW threshold. The blue and red arrows show the direction of the increase in the magnitude of the current pulses below and above CW threshold respectively. The inset shows a schematic of the current pulses supplied to the device in addition to the DC current. The lasing threshold, $\delta I_{pulse, Th}$, is indicated for both measurements.

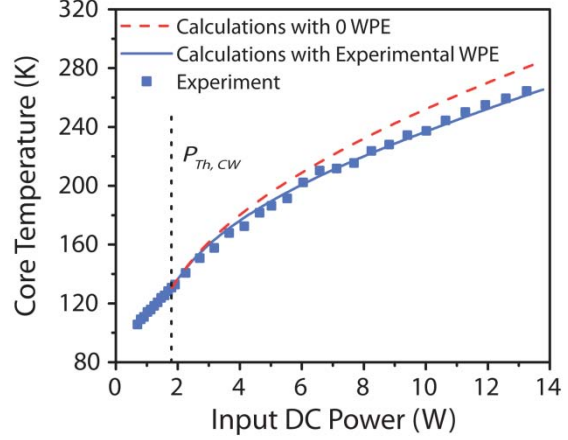


Fig. 34: Plot of core temperature versus DC input power. The blue squares are for the experimental results; the blue, solid line is for calculations including the WPE; and the red, dashed line is for calculations with zero WPE for all input powers. The power corresponding to CW threshold, $P_{DC, Th} = 1.8$ W, is marked by the vertical, dashed line. There is excellent agreement between experiment and the calculations; the only free parameter is the initial core temperature which was matched to the experiment.

$$\Delta T_{core}(T_{core}) = \Delta P_{DC} (1 - \eta_{WPE}(P_{DC})) R_{TH}(T_{core}) \quad (22)$$

where ΔP_{DC} is the change in applied DC power and η_{WPE} is the WPE. The increment in core temperature, ΔT_{core} , was added to the previously calculated temperature. As can be seen in Fig. 34, there is excellent agreement between the experimental data and the calculations.

To show the effect of large η_{WPE} on the temperature of the core, the same calculations were performed with $\eta_{WPE} = 0$ for all DC powers. The results are also shown in Fig. 34. Around $P_{DC} = 12$ W input power, the difference in core temperature is approximately 15 K. This difference in temperature is due to the efficient emission of light for this device. The size of the temperature difference is strongly influenced by R_{TH} and the reduction in R_{TH} at higher core temperatures limits the magnitude of the difference; at $P_{DC} = 12$ W, $R_{TH} \approx 9.3$ K/W.

In conclusion, we have measured the evolution of the core temperature and current efficiency of a QC laser in CW operation. The measured results agree well with calculations of the core temperature that use both the measured η_{WPE} and R_{TH} . Excluding η_{WPE} in the model results in an increase in the core temperature of 15 K at typical CW operating currents. The size of the temperature difference is strongly influenced by R_{TH} .

3. Discussion and recommendation

3.1. Discussion of results

In our initial approach to the Tasks under the EMIL program we closely followed our planned multi-faceted approach, addressing individual challenges and open questions regarding the various components of the WPE. We addressed essentially all Phase I issues, eliminating some as not essential, and/or resolving others. Ultimately, as outlined above, the biggest innovation and the greatest advancements came from the work on innovative injection designs, which improved voltage efficiency, internal efficiency, and also current efficiency (at low temperatures); only the optical efficiency was not systematically improved.

We demonstrated $\text{In}_{0.635}\text{Al}_{0.356}\text{As}/\text{In}_{0.678}\text{Ga}_{0.322}\text{As}$ strain compensated QC lasers that employ heterogeneous injector regions for low voltage defect operation. The active core consisted of interdigitated undoped and doped injectors followed by nominally identical wavelength optical transitions. The undoped injector regions were designed with reduced voltage defect while the doped injectors are of a more conventional design. The measured average voltage defect was less than 79 meV. At 80 K, a 2.3 mm long, back facet high reflectance coated laser had an emission wavelength of 4.7 μm and output 2.3 W pulsed power with a peak wall-plug efficiency of 19%.

We demonstrated a QC laser emitting at 4.2 μm featuring a low voltage defect and short injector with only four quantum wells. Devices with a voltage defect of 20 meV, well below the energy of the longitudinal optical phonons, and a voltage efficiency of 91%, a record value for QC lasers, were demonstrated for pulsed operation at 180 K. Voltage efficiencies of greater than 80% were still exhibited at room temperature. Overall performance showed WPE's ranging from 21% at cryogenic temperatures to 5.3% at room temperature.

The impact of the interface roughness on intersubband transitions in quantum wells was analyzed as an inhomogeneous broadening due to localization rather than a traditional scattering process. The results offered a simple explanation for the temperature dependent spectra of gain and absorption in QC lasers and pointed the way for improved designs as detailed in section 3.2 "Recommendation" below. In particular, a density-matrix based theory of transport and lasing in QC lasers revealed that the large disparity between luminescent linewidth and broadening of the tunneling transition changes the design guidelines to favor a stronger coupling between injector and upper laser level. This conclusion is supported by initial experimental evidence.

We furthermore calculated the intersubband absorption loss and measured the waveguide loss for two high-performance mid-infrared QC laser designs. We found, that intersubband absorption loss accounts for a major component of waveguide loss for these structures.

Finally, we devised more refined measurement techniques for the instantaneous core temperature of a QC laser. By superimposing low duty cycle current pulses on a core-heating DC baseline, we observed the instantaneous threshold current and current efficiency evolution as the DC input was varied. From these measurements we recovered the laser core temperature, T_{core} ; the results agreed well with calculations of T_{core} based on measured thermal resistance and WPE. Using the same model, we calculated that the large WPE of a specific high performing device, 24 % for 80 K heat sink, resulted in a core temperature reduction of ~15 K compared to a laser with negligible WPE.

3.2. Recommendation

Based on the insights of our Phase I work on QC laser injection regions with few quantum wells and our theoretical considerations of the transition broadening in QC lasers, we have recently devised a new strong-coupling injection scheme for QC lasers, which – even in its first embodiments – promises significant improvements in QC laser performance, especially in WPE and output power. The innovation resulted from a more efficient and faster electron injection process from the injector into the active region. As a result:

- (i) The *internal efficiency* increases as fewer electrons scatter into states other than the upper laser states.
- (ii) The *current efficiency* increases as the differential resistance is reduced and a higher current can be carried by the structure for the same amount of doping.
- (iii) The *voltage efficiency* is unchanged (i.e. not diminished over other approaches), as the injection process is independent of applied field and injector energy drop.
- (iv) The *optical efficiency* should not be affected or should potentially improve as less doping can be used.

Our initial results, outlined in more detail below and in Fig. 35, show highly promising results going towards 50% wall-plug efficiency in pulsed mode at low temperatures.

The improved QC laser design, shown in Fig. 35(A), employs a much stronger coupling (~ 20 meV), compared to conventional designs (~ 4 – 8 meV), between the injector ground level and the upper laser level. This is achieved by adopting much thinner injection barriers (~ 1 nm vs. ~ 3 – 4 nm in conventional designs) between the injector and the active regions. The ultra-strong coupling effectively overcomes the interface-roughness-induced detuning to the resonant tunneling, and leads to a more optimal tunneling current. Contrary to expectations, the ultra-strong coupling shows no negative impact on the gain profile (Fig 35(B)). The optical transition broadening is similar to that of the best comparable conventional designs.

Ridge-waveguide lasers are fabricated with widths varying from 13.5 – 21.5 μm using conventional processing techniques. Devices with lengths varying from 2.3 – 3.0 mm and as-cleaved facets are mounted epitaxial-side up to copper heat sinks. Experimental results show significant improvements in slope efficiency, peak power and WPE of the lasers. The laser spectrum is shown in Fig. 35(C). For pulsed mode operation (5 kHz repetition rate, 100 ns pulse width), the majority of the tested lasers have a peak wall-plug efficiency greater than 40% at 80 K. One of the best performing lasers has a slope efficiency of ~ 8 W/A, at least ~ 10 W peak output optical power (Fig. 35(D)) and a peak WPE of 47% at 80 K (Fig. 35(E)). The WPE increases to $>48\%$ at 9 K due to a slight decrease of the threshold current density. Taking into account the 0.45 Ω wiring resistance, the laser reaches 50% WPE at 9 K. These results are significant improvements compared to the best reported results [88], and surpass the performance limit predicted for conventional QC lasers in Ref. 89.

In summary, by employing an ultra-strong coupling between the injector and active regions to overcome the interface-roughness-induced detuning of resonant tunneling, this new design strategy greatly improved the QC laser WPE (from 34% to 50%).

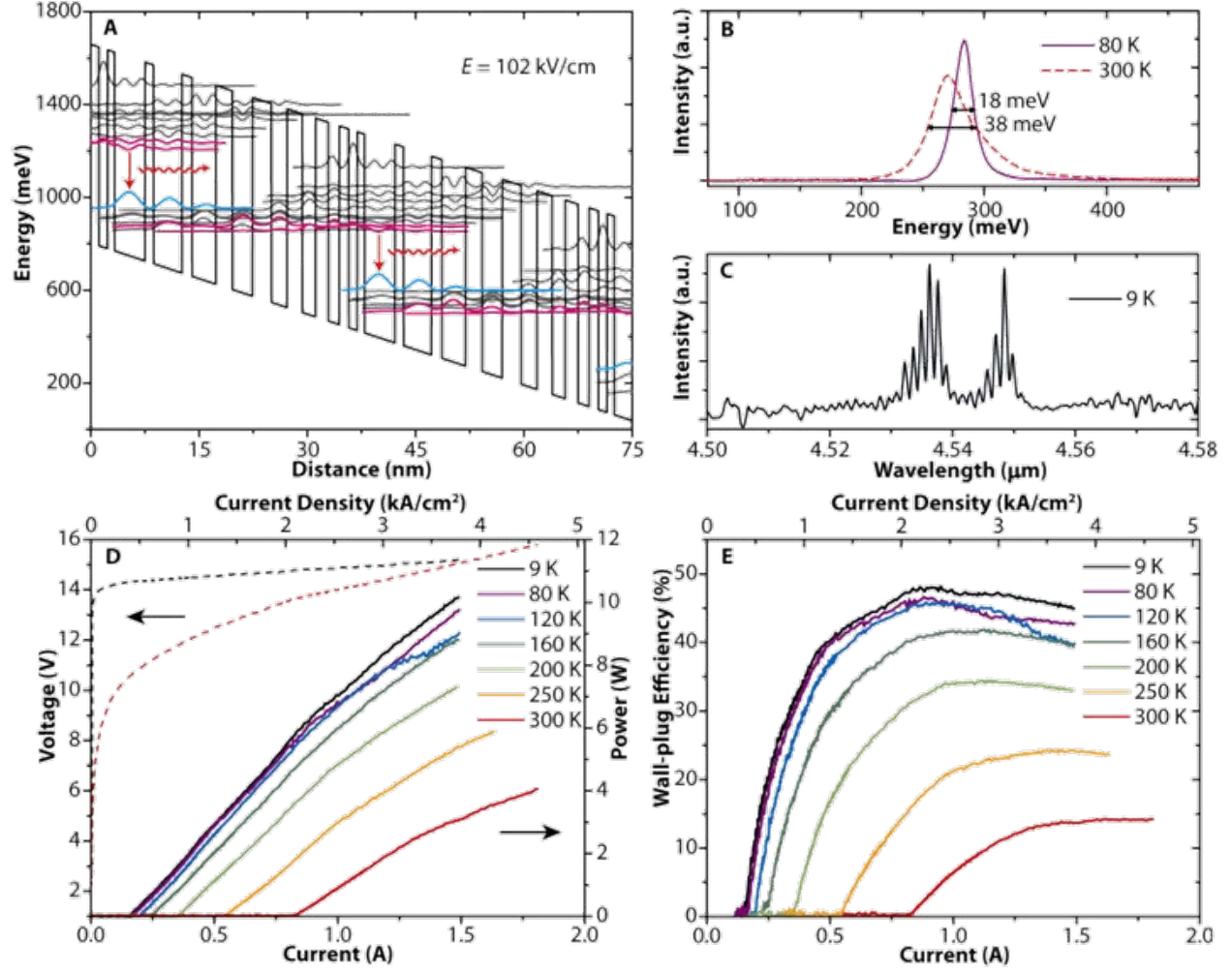


Fig. 35: (A) A portion of the conduction band diagram of the ultra-strong coupling QC laser design. The pairs of states in red have a coupling strength of ~ 20 meV. Starting from the first barrier in the injector, the layer sequence with individual thickness in nanometer is: 2.3/2.8/2.6/2.2/2.1/1.8/1.8/1.5/1.3/1.2/1.0/4.2/1.2/3.9/1.4/3.3, where the InAlAs barrier layers are in bold, the InGaAs well layers are in roman. (B) Electroluminescence spectra of the QC structure with extracted full width at half maximum. (C) Exemplary laser spectrum. (D) Pulsed light-current-voltage measurements for an as-cleaved $13.5 \mu\text{m}$ wide, 2.9 mm long QC laser at various heat sink temperatures. Measured single-facet optical power is doubled for two facets and corrected for optical collection efficiency. (E) Wall-plug efficiency extracted from the experimental results in (D).

Our recommendation is then to build upon these initial results, and to further explore, optimize, and adapt them for the overall improvement of QC lasers operating in CW-RT mode. In particular:

1. For the optimization of the strong-coupling injection scheme, we will optimize the coupling for the parameters of input coupling strength, doping density, and exit coupling strength. (So far, the concept was only applied to input coupling.)

2. For CW and/or RT operation, we will optimize the injector voltage drop to limit thermal backfilling, while retaining strong coupling.
3. As the amount of optimum strong-coupling depends on the interface roughness of the wells and barriers of the injector/active region interface, we will explore various regimes of roughness by growth.
4. For the optimization of the optical efficiency, we will re-evaluate and – as far as possible – reduce the optical loss, as well as apply coatings for optimum outcoupling.

The major improvement of the new injection scheme lies in the enhanced internal and current efficiency. Without strong coupling, values for these efficiencies reach ~ 0.75 and ~ 0.85 , at low temperatures, respectively, and significantly less at RT and/or CW operation. To reach 50% wall plug efficiency at room temperature and/or CW operation, the voltage efficiency will likely have to drop below 0.80 to counter thermal back-filling. As a result, the internal and current efficiency need to rise above 0.90; simultaneously, the outcoupling efficiency needs to rise to above 0.85 as well.

4. References

- [1] C. Gmachl, F. Capasso, A. Tredicucci, D. L. Sivco, R. Köhler, A. L. Hutchinson, and A. Y. Cho, *IEEE J. Select. Topics Quantum Electron.* 5, pp. 808 – 816 (May/June 1999).
- [2] J. Kim, M. Lerttamrab, S. L. Chuang, C. Gmachl, D. L. Sivco, F. Capasso, A. Y. Cho, *IEEE J. Quantum Electron.* 40, 1663 (2004).
- [3] J. Faist, F. Capasso, D. L. Sivco, A. L. Hutchinson, S.N.G. Chu, and A. Y. Cho, *Appl. Phys. Lett.* 72 (6), 680-682 (1998)
- [4] C. Gmachl, A. Michael Sergent, A. Tredicucci, F. Capasso, A. L. Hutchinson, D. L. Sivco, J. N. Baillargeon, S. N. G. Chu, and A. Y. Cho, *IEEE Photon. Techn. Lett.* 11, pp. 1369 – 1371 (1999).
- [5] Ph.D. Thesis, Scott Howard, Princeton University 2008; S. S. Howard, Z. Liu, and C. F. Gmachl, *IEEE J. Quantum Electron.*, vol. 44, no. 3-4, pp. 319–323, MAR-APR 2008.
- [6] Michael Weimer, Texas A&M University, private communication.
- [7] N.S. Wingreens, C.A. Stafford, *IEEE J. Quantum Electron.* 33 (7), 1170–1173 (1997) S. Anders, L. Rebohle, F.F. Schrey, W. Schrenk, K. Unterrainer, G. Strasser, *Appl. Phys. Lett.* 82 (22), 3862 – 3864 (2003). R.A. Suris, I.A. Dmitriev, *Physica Status Solidi A*, 202 (6), 987–991 (2005).
- [8] J. S. Yu, S. Slivken, A. Evans, J. David, and M. Razeghi, *Appl. Phys. Lett.* 82, 3397 (2003).
- [9] Vurgaftman and J. R. Meyer, *IEEE J. Quantum Electron.* 38, 592 (2002). W. W. Bewley, C. S. Kim, M. Kim, C. L. Canedy, J. R. Lindle, I. Vurgaftman, J. R. E. Muller, P. M. Echternach, and R. Kaspi, *Appl. Phys. Lett.* 83, 5383 (2003). S. Kim, W. W. Bewley, C. L. Canedy, I. Vurgaftman, M. Kim, and J. R. Technol. Lett. 16, 1250 (2004).
- [10] J. R. Leger, Chapter 8 in *Surface Emitting Semiconductor Lasers and Arrays*, G. A. Evans and J. M. Hammer, eds., (Academic, Boston, 2003). T. Y. Fan, *IEEE J. Select. Top. Quantum Electron.* 11, 567 (2005).
- [11] Evans, J. S. Yu, S. Slivken, and M. Razeghi, *Appl. Phys. Lett.* 85, 2166 (2004) W. W. Bewley, J. R. Lindle, C. S. Kim, I. Vurgaftman, J. R. Meyer, A. J. Evans, J. S. Slivken, and M. Razeghi, *IEEE J. Quantum Electron.* 41, 833 (2005). A. Evans, J. Nguyen, S. Slivken, J. S. Yu, S. R. Darvish, and M. Razeghi, *Appl. Phys. Lett.* 88, 051105 (2006). L. Diehl, D. Bour, S. Corzine, J. Zhu, G. Hofler, B. G. Lee, C. Y. Wang, M. Troccoli, and F. Capasso, *Appl. Phys. Lett.* 88, 041102 (2006).
- [12] Vurgaftman and J.R. Meyer, "Analysis of limitations to wallplug efficiency and output power from quantum cascade lasers," *J. Appl. Phys.* 99, 123108 (2006).
- [13] J. Faist, *Appl. Phys. Lett.* 90, 253512 (2007).
- [14] Zhijun Liu, Claire F. Gmachl, Liwei Cheng, Fow-Sen Choa, Fred J. Towner, Xiaojun Wang and Jenyu Fan, *IEEE Journal of Quantum Electronics* 44 (5) 485-492 (2008).
- [15] J. Nguyen, J.S. Yu, A. Evans, S. Slivken and M. Razeghi, *Appl. Phys. Lett.* 89, 111113 (2006).

- [16] Tsekoun, R. Go, M. Pushkarsky, M. Razeghi and C.K.N. Patel, PNAS 103, 4831 - 4835 (2006).
- [17] Evans, S.R. Darvish, S. Slivken, J. Nguyen, Y. Bai and M. Razeghi, Appl. Phys. Lett. 91, 071101 (2007).
- [18] J.S. Yu, S.R. Darvish, A. Evans, J. Nguyen, S. Slivken and M. Razeghi, Appl. Phys. Lett. 88, 041111 (2006).
- [19] Evans, J.S. Yu, J. David, L. Doris, K. Mi, S. Slivken and M. Razeghi, Appl. Phys. Lett. 84, 314 - 316 (2004).
- [20] Evans, J.S. Yu, S. Slivken and M. Razeghi, Appl. Phys. Lett. 85, 2166 -2168 (2004).
- [21] M. D. Escarra, S. S. Howard, A. J. Hoffman, X. Wang, and C. Gmachl, (unpublished).
- [22] J. Hoffman, S. Scharfner, S. S. Howard, K. J. Franz, F. Towner, and C. Gmachl, Opt. Express 15, 15818 (2007).
- [23] M. C. Wanke, F. Capasso, C. Gmachl, A. Tredicucci, D. L. Sivco, A. L. Hutchinson, S. N. G. Chu, and A. Y. Cho, Appl. Phys. Lett. 78, 25 (2001).
- [24] S. Katz, A. Vizbaras, G. Boehm, and M.-C. Amann, Appl. Phys. Lett. 94, 151106 (2009).
- [25] D. Dey, W. Wu, O. G. Memis, and H. Mohseni, Appl. Phys. Lett. 94, 081109 (2009).
- [26] K. J. Nash, M. S. Skolnick, and S. J. Bass, Semicond. Sci. Technol. 2, 329 (1987).
- [27] Y. Bai, S. Slivken, S. R. Darvish, and M. Razeghi, Appl. Phys. Lett. 93, 021103 (2008).
- [28] Evan, S. R. Darvish, S. Slivken, J. Nguyen, Y. Bai, and M. Razeghi, Appl. Phys. Lett. 91, 071101 (2007).
- [29] Z. Liu, C. F. Gmachl, L. Cheng, F. S. Choa, F. J. Towner, X. Wang, and J. Fan, IEEE J. Quantum Electron. 44, 485 (2008).
- [30] J. B. Khurgin, Y. Dikmelik, P. Q. Liu, A. J. Hoffman, M. D. Escarra, K. J. Franz, and C. F. Gmachl, Appl. Phys. Lett. 94, 091101 (2009).
- [31] Lyakh, C. Pflügl, L. Diehl, Q. J. Wang, F. Capasso, X. J. Wang, J. Y. Fan, T. Tanbun-Ek, R. Maulini, A. Tsekoun, R. Go, and C. K. N. Patel, Appl. Phys. Lett., vol. 92, p. 111110, 2008.
- [32] M. Razeghi, "High-power high-wall plug efficiency mid-infrared quantum cascade lasers based on InP/GaInAs/InAlAs material system," A. A. Belyanin and P. M. Smowton, Eds., vol. 7230, no. 1. SPIE, 2009, p. 723011.
- [33] D. Hofstetter, M. Beck, T. Aellen, and J. Faist, Appl. Phys. Lett., vol. 78, no. 4, pp. 396–398, 2001.

- [34] M. Beck, D. Hofstetter, T. Aellen, J. Faist, U. Oesterle, M. Illegems, E. Gini, and H. Melchior, *Science*, vol. 295, no. 5553, pp. 301–305, 2002.
- [35] M. C. Wanke, F. Capasso, C. Gmachl, A. Tredicucci, D. L. Sivco, A. L. Hutchinson, S.-N. G. Chu, and A. Y. Cho, “Injectorless quantum-cascade lasers,” *Appl. Phys. Lett.*, vol. 78, pp. 3950–3952, 2001.
- [36] Friedrich, G. Boehm, and M. C. Amann, *Semicond. Sci. Technol.*, vol. 22, pp. 218–221, 2007.
- [37] S. Katz, A. Friedrich, G. Boehm, and M.-C. Amann, *Appl. Phys. Lett.*, vol. 92, p. 181103, 2008.
- [38] Sirtori, F. Capasso, J. Faist, A. Hutchinson, D. Sivco, and A. Cho, *IEEE J. Quantum Electron.*, vol. 34, no. 9, pp. 1722–1729, Sep 1998.
- [39] T. Aellen, M. Beck, N. Hoyler, M. Giovannini, J. Faist, and E. Gini, *J. Appl. Phys.*, vol. 100, no. 4, p. 043101, 2006.
- [40] K. J. Franz, D. Wasserman, A. J. Hoffman, D. C. Jangraw, K.-T. Shiu, S. R. Forrest, and C. Gmachl, *Appl. Phys. Lett.*, vol. 90, no. 9, p. 091104, 2007.
- [41] K. Leo, *High-Field Transport in Semiconductor Superlattices*. Berlin: Springer, 2006.
- [42] P. G. Savvidis, B. Kolasa, G. Lee, and S. J. Allen, *Phys. Rev. Lett.*, vol. 92, no. 19, p. 196802, May 2004.
- [43] M. D. Escarra, A. J. Hoffman, K. J. Franz, S. S. Howard, R. Cendejas, X. Wang, J.-Y. Fan, and C. Gmachl, *Appl. Phys. Lett.*, vol. 94, no. 25, p. 251114, 2009.
- [44] “Intersubband Transitions in Quantum structures”, R. Paella, Editor, McGraw-Hill, NY (2006)
- [45] J. Faist, F. Capasso, D. L. Sivco, C. Sirtori, A. L. Hutchinson, and A. Y. Cho, *Science* 264, 553 (1994).
- [46] T. Unuma, T. Takayashi, T. Noda, M. Yoshida, *Appl. Phys. Lett.*, 78, 3448 (2001)
- [47] K. L. Chapman, H. Schmidt, A. Imamoglu, A. C. Gossard, *Appl. Phys. Lett.*, 69, 2554 (1996)
- [48] S. Tsujino, A. Borak, E. Müller, M. Scheinert, C. V. Falub, H. Sigg, D. Grützmacher, M. Giovannini and J. Faist *Appl. Phys. Lett* 86, 062113 (2005)
- [49] T. Ando, A. B. Fowler, *F. Stern Rev. Mod. Phys.*, 54, 437 (1982)
- [50] T. Ando, *J. Phys. Soc. Jpn.* 54, 2671 (1985)
- [51] V. Gorfinkel., S. Luryi, B. Gelmont, *IEEE J. Quantum Electron.* 32, 1995–2003 (1996).
- [52] F. T. Vasko, P. Aceituno, A. Hernandez-Cabrera, *Phys. Rev. B* 66, 125303 (2002)
- [53] H. Willenberg, G. H. Dohler and J. Faist *Phys. Rev. B* 67 085315 (2003)

- [54] Wacker, Phys. Rev. B 66 085326 (2002)
- [55] R. Terazzi, T. Gresch, M. Giovannini, N. Hoyler, J. Faist, and N. Sekine, Nat. Phys. 3, 329 (2007).
- [56] G. Revin, M. R. Soulby, J. W. Cokburn, Q. Yang, C. Manz and J. Wagner Appl. Phys. Lett, 92,081110 (2008)
- [57] R. Kubo, J. Phys. Soc. Jpn, 12, 570 (1957)
- [58] A. Greenwood, Proc. Phys. Soc., 71, 585 (1958)
- [59] Ciuti, G. Bastard, I. Carusotto, Phys. Rev. B 72, 115303 (2005) ;
- [60] A. Anappara, A. Tredicucci, F. Beltram, G. Biasiol, L. Sorba, S. De Liberato, C. Ciuti, Appl. Phys. Lett. 91, 231118 (2007)
- [61] R. Colombelli, C. Ciuti, Y. Chassagneux, and C. Sirtori, Semicond. Science and Tech., 20, 985 (2005).
- [62] S. De Liberato, C. Ciuti, Phys. Rev. B 77, 155321 (2008)
- [63] Dini, R. Köhler, A. Tredicucci, G. Biasiol, and L. Sorba, Phys. Rev. Lett. 90, 116401 (2003).
- [64] Hofstetter, M. Beck, T. Aellen, and J. Faist, Appl. Phys. Lett. 78, 396 (2001).
- [65] J. Faist, M. Beck, T. Aellen, and E. Gini, Appl. Phys. Lett. 78, 147 (2001)
- [66] R. F. Kazarinov and R. A. Suris, Sov. Phys. Semicond., 5, pp. 707–709, (1971)
- [67] J. Faist, Appl. Phys. Lett, 90, 253512, (2007)
- [68] C. Sirtori, Federico Capasso, J. Faist, A. L. Hutchinson, D. L. Sivco, and A. Y. Cho, IEEE J. Quantum Electron., 34, pp. 1722-1729 (1998).
- [69] R. F. Kazarinov and R. A. Suris, Sov. Phys. Semicond., 5, pp. 707–709, 1971)
- [70] A. Wittmann, Y. Bonetti, J. Faist, E. Gini, M. Giovannini, Appl. Phys. Lett, 93, 141103 (2008)
- [71] S. Tsujino, A. Borak, E. Müller, M. Scheinert, C. V. Falub, H. Sigg, D. Grützmacher, M. Giovannini and J. Faist, Appl. Phys. Lett 86, 062113 (2005)
- [72] J. B. Khurgin, Appl. Phys. Lett 93, 091104 (2008)
- [73] P. Liu, et al., “Quantum cascade lasers with ultra-strong coupling injection design,” Appl. Phys. Lett. (in preparation)
- [74] H. Schmidt, K. L. Campman, A. C. Gossard, and A. Imamoglu, Appl. Phys. Lett 70, 3455 (1997)

- [75] Lyakh, C. Pflugl, L. Diehl, Q. J. Wang, F. Capasso, X. J. Wang, J. Y. Fan, T. Tanbun-Ek, R. Maulini, A. Tsekoun, R. Go, and C. K. N. Patel, *Appl. Phys. Lett.*, 92, 111110 (2008).
- [76] J. Faist, *Appl. Phys. Lett.*, 90, 253512 (2007).
- [77] Z. Liu, C. F. Gmachl, L. Cheng, F. S. Choa, F. J. Towner, X. Wang, and J. Fan, *IEEE J. Quantum Electron.*, 44, 485 (2008).
- [78] S. Tsujino, A. Borak, E. Muller, M. Scheinert, C. V. Falub, H. Sigg, D. Grutzmacher, M. Giovannini, and J. Faist, *Appl. Phys. Lett.*, 86, 062113 (2005).
- [79] J. B. Khurgin, *Appl. Phys. Lett.*, 93, 091104 (2008).
- [80] Evan, S. R. Darvish, S. Slivken, J. Nguyen, Y. Bai, and M. Razeghi, *Appl. Phys. Lett.* 91, 071101 (2007). Y. Bai, S. R. Darvish, S. Slivken, W. Zhang, A. Evans, J. Nguyen, and M. Razeghi, *Appl. Phys. Lett.* 92, 101105 (2008). A. Lyakh, C. Pflugl, L. Diehl, Q. J. Wang, F. Capasso, X. J. Wang, J. Y. Fan, T. Tanbun-Ek, R. Maulini, A. Tsekoun, R. Go, and C. K. N. Patel, *Appl. Phys. Lett.* 92, 111110 (2008). Y. Bai, S. Slivken, S. R. Darvish, and M. Razeghi, *Appl. Phys. Lett.* 93, 021103 (2008).
- [81] S. S. Howard, Z. Liu, D. Wasserman, A. J. Hoffman, T. S. Ko, and C. F. Gmachl, *IEEE J. Sel. Topics Quantum Electron.* 13, 1054 (2007). S. S. Howard, Z. Liu, and C. F. Gmachl, *IEEE J. Quantum Electron.* 44, 319 (2008). A. Wittman, Y. Bonetti, J. Faist, E. Gini, and M. Giovannini, *Appl. Phys. Lett.* 93, 141103 (2008).
- [82] J. Hoffman, S. Scharfner, S. S. Howard, K. J. Franz, F. Towner, and C. Gmachl, *Opt. Express* 15, 15818 (2007).
- [83] M. Beck, D. Hofstetter, T. Aellen, J. Faist, U. Oesterle, M. Illegems, E. Gini, and H. Melchior, *Science* 295, 301 (2002).
- [84] C. Pflugl, M. Litzenberger, W. Schrenk, D. Pogany, E. Gornik, and G. Strasser, *Appl. Phys. Lett.* 82, 1664 (2003).
- [85] V. Spagnolo, M. Troccoli, G. Scamarcio, C. Gmachl, F. Capasso, A. Tredicucci, A. M. Sergent, A. L. Hutchinson, D. L. Sivco, and A. Y. Cho, *Appl. Phys. Lett.* 78, 2095 (2001).
- [86] V. Spagnolo, G. Scamarcio, H. Page, and C. Sirtori, *Appl. Phys. Lett.* 84, 3690 (2004).
- [87] S. Katz, A. Friedrich, G. Boehm, and M.-C. Amann, *Appl. Phys. Lett.* 92, 181103 (2008).
- [88] J. Khurgin, et al., *Appl. Phys. Lett.* 94, 091101 (2009)
- [89] C. Sirtori, et al., *IEEE J. Quantum Electron.* 34, 1722 (1998)